Delft University of Technology

Multiscale finite-element method for linear elastic geomechanics

Castelletto, N; Hajibeygi, Hadi; Tchelepi, HA

Important note
To cite this publication, please use the final published version (if applicable).
Please check the document version above.

Accepted Manuscript

Multiscale finite-element method for linear elastic geomechanics

Nicola Castelletto, Hadi Hajibeygi, Hamdi A. Tchelepi

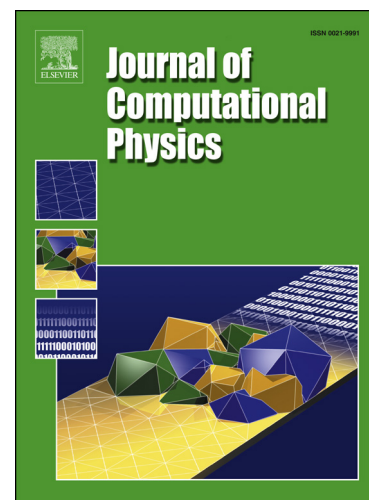Please cite this article in press as: N. Castelletto et al., Multiscale finite-element method for linear elastic geomechanics, *J. Comput. Phys.* (2016), http://dx.doi.org/10.1016/j.jcp.2016.11.044

Multiscale Finite-Element Method for Linear Elastic Geomechanics

Nicola Castelletto[a,*], Hadi Hajibeygi[b], Hamdi A. Tchelepi[a]

[a]*Department of Energy Resources Engineering, Stanford University, Stanford, CA, USA*
[b]*Department of Geoscience and Engineering, Faculty of Civil Engineering and Geosciences, Delft University of Technology, Delft, The Netherlands*

Abstract

The demand for accurate and efficient simulation of geomechanical effects is widely increasing in the geoscience community. High resolution characterizations of the mechanical properties of subsurface formations are essential for improving modeling predictions. Such detailed descriptions impose severe computational challenges and motivate the development of multiscale solution strategies. We propose a multiscale solution framework for the geomechanical equilibrium problem of heterogeneous porous media based on the finite-element method. After imposing a coarse-scale grid on the given fine-scale problem, the coarse-scale basis functions are obtained by solving local equilibrium problems within coarse elements. These basis functions form the restriction and prolongation operators used to obtain the coarse-scale system for the displacement-vector. Then, a two-stage preconditioner that couples the multiscale system with a smoother is derived for the iterative solution of the fine-scale linear system. Various numerical experiments are presented to demonstrate accuracy and robustness of the method.

Keywords: Multiscale methods, multiscale finite-element method, geomechanics, preconditioning, porous media.

1. Introduction

Geomechanical effects play a crucial role in many geoscience applications involving significant fluid withdrawal and injection in the subsurface, both from the effective design and environmental safety assessment perspectives. Application areas include unconventional hydrocarbon reservoirs, hydraulic fracturing operations, geothermal systems, geological carbon storage, and waste-water disposal. Safe and optimized field operations are highly dependent on accurate and efficient numerical simulations. The mathematical formulation that describes the deformation of a geological formation, typically coupled with flow and transport processes, entails heterogeneous coefficients over a wide range of length scales, thus high-resolution computational grids are required. Such detailed descriptions of hydro-mechanical properties impose severe computational challenges, and motivate the development of multiscale solution strategies.

MultiScale Finite-Volume (MSFV) methods [1, 2] have been developed as a conservative reformulation of its finite-element counterpart [3, 4] for subsurface flow and transport simulation. Recent advancements of the method include iterative error reduction strategies within an algebraic framework, complex nonlinear compressibility and compositional fluid physics, adaptive flow-transport simulation strategies, flow and transport in fractured/faulted media with complex wells, and reservoir models with unstructured grids—see, e.g., [5–10] and references therein. All of these important developments have made the method to be a promising approach for next-generation subsurface simulation [11].

Within the upscaling framework, the MultiScale Finite-Element (MSFE) method has been applied to the vector partial differential equations for the elasticity problem [4]. Applications to consolidation of heterogeneous porous media and elasto-plastic analysis of heterogeneous material are discussed in [12–14]. Beyond the original idea of

---

*Corresponding author.

Email addresses: `ncastell@stanford.edu` (Nicola Castelletto), `h.hajibeygi@tudelft.nl` (Hadi Hajibeygi), `tchelepi@stanford.edu` (Hamdi A. Tchelepi)

multiscale methods, namely providing approximate solutions at low computational cost, the multiscale basis functions allow for the construction of coarse-spaces that can be used as effective coarse-grid solvers in two-level domain decomposition preconditioners [15]. Recent applications to linear elasticity based on additive Schwarz preconditioning include [16–18], the focus being mainly on the construction of robust coarse-spaces with respect to material parameters heterogeneities.

The primary objective of the present work is to extend the Algebraic Multiscale Solver (AMS) for flow presented in [9, 19] to the mechanical response of heterogeneous elastic geological porous media. Based upon a standard FE fine-scale system [20], we show that the framework developed for flow through porous media can be naturally generalized to the geomechanical equilibrium problem. By imposing a coarse-scale grid, which is a non-overlapping decomposition of the domain, local basis functions are computed for the displacement field via a physically-based approach that introduces local equilibrium problems within coarse elements. In particular, basis functions for the displacement-vector are solved subject to localization conditions, namely, reduced-dimensional boundary conditions. If a *wire-basket* decomposition of the fine-scale problem [21] is introduced—namely, a hierarchical partitioning of the fine-scale unknowns associated with coarse-scale grid faces, edges and vertices, respectively—, the localization conditions can be formalized algebraically as local approximations to the Schur complement on coarse-scale element interfaces (edges, faces). The basis functions provide prolongation and restriction operators used to obtain a MSFE formulation at the coarse-scale. While local basis functions allow for the construction of accurate prolongation and restriction operators, challenging problems require improving the quality of the multiscale solutions iteratively. In addition, a scalable iterative approach for the multiscale formulation allows for maintaining the quality of the solutions to the level of a user-defined threshold. Therefore, in this work, the devised multiscale method is combined with a second-stage smoother. The quality of the developed multiscale method with and without iterations is tested for several cases. The examples include heterogeneous material parameters on distorted mesh and several loading/boundary conditions. Numerical evidence shows that the proposed multiscale method is robust and accurate for modeling the deformation of large-scale subsurface formations. It is a significant step forward in the formulation and application of multiscale methods for modeling and simulation of subsurface formations accounting for geomechanical effects.

The paper is organized as follows. After a brief review of the model equations and the fine-scale discrete system in Section 2, the multiscale formulation is presented in Section 3. First, we describe the construction of the multiscale basis functions, which provide the prolongation and restriction operators used to obtain the coarse-scale systems for the displacement. A two-stage preconditioner, which couples the multiscale system with a smoother, is then derived for the iterative solution of the fine-scale linear system. In Section 4, numerical experiments, addressing the deformation a synthetic heterogeneous layered porous medium and a real-life plane strain subsidence model, are presented. This systematic study illustrates the accuracy and robustness of the method with respect to distorted mesh, material anisotropy and boundary/loading conditions. The paper is concluded in Section 5.

2. Fine-scale Model

2.1. Governing equations

Let $\Omega \subset \mathbb{R}^{n_{\dim}}$ and Γ denote the porous medium and its boundary, respectively, with x the position vector in $\mathbb{R}^{n_{\dim}}$ and $n_{\dim} = 1, 2,$ or 3 the spatial dimension of the problem. The boundary of the domain, Γ, is decomposed as $\Gamma = \overline{\Gamma_u \cup \Gamma_\sigma}$, with $\Gamma_u \cap \Gamma_\sigma = \emptyset$, and n denotes its outer normal-vector. Let $u : \overline{\Omega} \to \mathbb{R}^{n_{\dim}}$ be the displacement-vector. Under quasi-static conditions, the solution of the linear-momentum balance equation is the function u that satisfies the boundary value problem [22]:

$$\nabla \cdot \sigma = 0 \qquad \text{in } \Omega \qquad \text{(equilibrium equations)}, \qquad (1a)$$

$$u = \bar{u} \qquad \text{on } \Gamma_u \qquad \text{(prescribed boundary displacements)}, \qquad (1b)$$

$$\sigma \cdot n = \bar{t} \qquad \text{on } \Gamma_\sigma \qquad \text{(prescribed boundary tractions)}, \qquad (1c)$$

with σ the rank-2 stress tensor increment relative to an initial reference state; $\bar{u} : \Gamma_u \to \mathbb{R}^{n_{\dim}}$ and $\bar{t} : \Gamma_\sigma \to \mathbb{R}^{n_{\dim}}$ known functions; and $(\nabla \cdot)$ the divergence operator. Assuming a linear elastic constitutive model, the rank-4 elasticity tensor, $\mathbf{C}_{dr}$, relates σ to u via the linearized second-order strain tensor, ϵ, namely,

$$\sigma = \mathbf{C}_{dr} : \epsilon, \tag{2}$$

$$\epsilon = \nabla^s u = \frac{1}{2} \left(\nabla u + \nabla^T u \right), \tag{3}$$

where ∇ and ∇^s are the gradient and symmetric gradient operator, respectively, and (:) denotes a tensor product contracted on two indices. For isotropic media, $\mathbf{C}_{dr}$ depends on two coefficients only, e.g. Young's modulus, E, and Poisson's ratio, ν. Combining Equations (1a), (2) and (3), the linear-momentum balance equation is expressed using u as primary unknown, i.e.,

$$\nabla \cdot (\mathbf{C}_{dr} : \nabla^s u) = \mathbf{0}. \tag{4}$$

2.2. Variational formulation

The discretization of the the boundary value problem (1) is obtained by the Galerkin FE method, based on the standard variational form of (1a). The following spaces are introduced for the trial ($\mathcal{S}$) and test ($\mathcal{V}$) functions:

$$\mathcal{S}(\Omega) := \left\{ u \mid u \in [H^1(\Omega)]^{n_{\dim}}, u = \bar{u} \text{ on } \Gamma_u \right\}, \tag{5}$$

$$\mathcal{V}(\Omega) := \left\{ w \mid w \in [H^1(\Omega)]^{n_{\dim}}, w = \mathbf{0} \text{ on } \Gamma_u \right\}, \tag{6}$$

with $H^1(\Omega)$ a Sobolev space of degree one. The weak form of the problem is to find $u \in \mathcal{S}(\Omega)$ such that

$$\int_{\Omega} \nabla^s w : \mathbf{C}_{dr} : \nabla^s u \, d\Omega - \int_{\Gamma_\sigma} w \cdot \bar{t} \, d\Gamma = 0 \quad \forall w \in \mathcal{V}(\Omega). \tag{7}$$

A partition $\mathcal{T}^h$ of Ω consisting of non-overlapping elements, T, is defined, on which the following discrete trial ($\mathcal{S}^h$) and weighting ($\mathcal{V}^h$) spaces are introduced:

$$\mathcal{S}^h := \left\{ u \mid u \in [C^0(\Omega)]^{n_{\dim}}, u = \bar{u} \text{ on } \Gamma_u, u_{|T^e} \in [Q_1(T)]^{n_{\dim}} \, \forall T \in \mathcal{T}^h \right\}, \tag{8}$$

$$\mathcal{V}^h := \left\{ w \mid w \in [C^0(\Omega)]^{n_{\dim}}, w = \mathbf{0} \text{ on } \Gamma_u, w_{|\Omega^e} \in [Q_1(T)]^{n_{\dim}} \, \forall T \in \mathcal{T}^h \right\}, \tag{9}$$

with $Q_1(T)$ the space of linear ($n_{\dim} = 1$), bilinear ($n_{\dim} = 2$), or trilinear ($n_{\dim} = 3$) polynomials in each element T. The discrete variational form of the problem is: find $u^h \in \mathcal{S}^h$ such that

$$\int_{\Omega} \nabla^s w^h : \mathbf{C}_{dr} : \nabla^s u^h \, d\Omega - \int_{\Gamma_\sigma} w^h \cdot \bar{t} \, d\Gamma = 0 \quad \forall w^h \in \mathcal{V}^h. \tag{10}$$

The displacement field is approximated as follows:

$$u^h = \sum_{i=1}^{n_u^h} d_i^h N_i^h + \sum_{i=1}^{n_{\bar{u}}^h} \bar{d}_i^h N_{i+n_u}^h, \tag{11}$$

where n_u^h is the number of nodal displacement degrees of freedom (DOFs), d_i^h, contained in vector d^h, $n_{\bar{u}}^h$ is the number of prescribed nodal displacement DOFs, $\bar{d}_i^h$, over Γ_u contained in vector $\bar{d}^h$, and N_i^h are the FE shape functions for $\mathcal{S}^h$. The matrix form of the equilibrium equations can be expressed as

$$K_h d^h = f^h, \tag{12}$$

where K_h and f^h are the stiffness matrix and global load vector, respectively, which are given by:
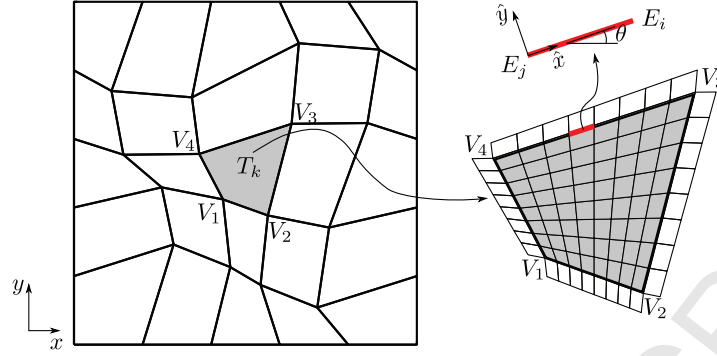
3

Figure 1: Two-dimensional multiscale grid: coarse grid $\mathcal{T}^H$ in bold lines (left) and fine grid $\mathcal{T}^h$ detail for the grey coarse element $T_k \in \mathcal{T}^H$ in thin lines (right).

$$[K_h]_{i,j} = \int_\Omega \nabla^s N_i^h : \mathbf{C}_{dr} : \nabla^s N_j^h \; d\Omega \qquad \forall (i,j) \in \left\{1, 2, \ldots, n_u^h\right\} \times \left\{1, 2, \ldots, n_u^h\right\}, \tag{13}$$

$$[f^h]_i = \int_{\Gamma_\sigma} N_i^h \cdot \bar{t} \; d\Gamma - [\bar{K}_h \bar{d}^h]_i \qquad \forall i \in \left\{1, 2, \ldots, n_u^h\right\}, \tag{14}$$

with

$$[\bar{K}_h]_{i,(j-n^u)} = \int_\Omega \nabla^s N_i^h : \mathbf{C}_{dr} : \nabla^s N_j^h \; d\Omega \qquad \forall (i,j) \in \left\{1, 2, \ldots, n_u^h\right\} \times \left\{n_u^h + 1, 2, \ldots, n_u^h + n_{\bar{u}}^h\right\}. \tag{15}$$

3. Multiscale Formulation

The MSFE formulation for displacement field is described. Then, a two-stage iterative procedure to maintain the desired multiscale vectorial solution quality is presented. An algebraic description of the basis function calculation (prolongation operator) is also described.

3.1. MSFE Model

The MSFE method is based on a two-grid approach. A coarse mesh $\mathcal{T}^H$ is superimposed on the given fine-scale grid $\mathcal{T}^h$, where the mechanical properties are described. Elements in $\mathcal{T}^H$ are aggregates of fine-scale elements. An illustration of the MSFE grid is given in Figure 1. The MSFE method approximates the fine-scale displacement-vector, i.e., the solution of equation (12), using the superposition expression

$$u^h \approx u_{MS}^h = \sum_{i=1}^{n_u^H} d_i^H N_i^H(x) + \sum_{i=1}^{n_{\bar{u}}^H} \bar{d}_i^H N_{i+n_u^H}^H, \tag{16}$$

with $N_i^H, i = 1, \ldots, (n_u^H + n_{\bar{u}}^H)$, the set of coarse-scale basis functions. Each function N_i^H is associated to a coarse nodal DOF and is computed locally over a coarse element $T_k \in \mathcal{T}^H$. The n_u^H unknown and $n_{\bar{u}}^H$ prescribed (Dirichlet) coarse-scale DOFs are collected in vectors d^H and $\bar{d}^H$, respectively.

Each basis function $N_i^H, i = 1, \ldots, n_u^H$, is a solution of the governing equations for the displacement-vector obtained by solving the following local Dirichlet linear-momentum balance problem on each coarse element T_k. That

4

is,

$$\nabla \cdot \left(\mathbf{C}_{dr} : \nabla^s \boldsymbol{N}_i^H \right) = \mathbf{0} \qquad \text{in } T_k, \tag{17a}$$

$$\nabla_{\parallel} \cdot \left(\mathbf{C}_{dr} : \nabla_{\parallel}^s \boldsymbol{N}_i^H \right) = \mathbf{0} \qquad \text{on } \partial T_k \setminus \Gamma_{\boldsymbol{u}}, \tag{17b}$$

$$\boldsymbol{N}_i^H = \mathbf{0} \qquad \text{on } \partial T_k \cap \Gamma_{\boldsymbol{u}}, \tag{17c}$$

$$\boldsymbol{N}_i^H(\boldsymbol{x}_j) = \delta_{ij}\, \boldsymbol{e} \qquad \forall j \in \left\{ 1, \ldots, n_{\boldsymbol{u}}^H \right\} \tag{17d}$$

where δ_{ij} is the Kronecker delta, $\boldsymbol{x}_j$ is the position vector of the coarse mesh node associated to the j-th unknown DOF, and $\boldsymbol{e}$ is the unit-vector in the coordinate direction associated with the i-th unknown DOF. Equation (17b) imposes a reduced-dimensional condition at the boundary of the coarse element for the displacement-vector. In Eq. (17b) $(\nabla_{\parallel} \cdot)$ and $\nabla_{\parallel}^s$ denote approximate divergence and symmetric gradient operators, respectively, acting in the tangential direction of the coarse elements boundary only, i.e., in a local reference system as shown in Fig.1 terms involving partial derivatives in directions normal to ∂T_k are neglected. The rationale underlying the localization assumption (17b) is the same as that used in the MSFE method for flow in porous media proposed in [3]. Appendix A provides detailed expressions for the plane-strain case, where the physical meaning of approximation (17b) is that coarse mesh edges are regarded as line elements for which only axial extension and transverse simple shear effects are accounted for. Also, as stated in Eq. (17c), over coarse-element boundaries that overlap with the external boundary of the global domain subject to a Dirichlet condition $\Gamma_{\boldsymbol{u}}$, the basis functions are set to zero. This is due to the fact that Dirichlet conditions on the global domain boundaries are captured employing supplementary basis functions $(\boldsymbol{N}_i^H, i = n_{\boldsymbol{u}}^H + 1, \ldots, n_{\boldsymbol{u}}^H + n_{\bar{\boldsymbol{u}}}^H)$, obtained by a similar procedure with Eq. (17c) suitably modified to interpolate Eq. (1b). Note that if the mechanical parameters are not uniquely defined at the boundaries of local domains ∂T_k, an averaging procedure must be employed. An illustration of basis functions is provided in Fig. 2. Notice that the approximate solution in each direction, e.g., x, is obtained by employing basis functions in both the x- and y-direction, as described in the superposition expression (16). Thus, expression (16) introduces additional coupling compared to standard FEs in which the displacement field in each direction is represented as a linear combination of nodal displacement in the corresponding direction only.

Remark 3.1. The extension to the three-dimensional (3D) case requires: (1) the solution of reduced problems on coarse element edges in a 3D setup, and (2) the solution of additional reduced problems on coarse element faces. Again, appropriate averaging criteria must be used to define properties over edges and faces in heterogeneous regions. Also, in analogy with the two-dimensional case, the operators $\nabla_{\parallel} \cdot$ and $\nabla_{\parallel}^s$ defined over coarse faces act in the tangential direction of the coarse element face, neglecting the terms involving partial derivatives in the direction normal to the face. If arbitrarily-distorted hexahedral meshes are adopted faces are generally non-planar and special care in computing surface integral is needed. On the other hand, tetrahedral grids do not involve additional difficulties compared to the two-dimensional case [17].

The coarse-scale basis functions can be expressed in functional form based on the fine-scale FE basis functions for $\mathcal{S}^h$. In particular, $\boldsymbol{N}_i^H = \sum_{k=1}^{n_{\boldsymbol{u}}^h} p_{i_k} \boldsymbol{N}_k^h$, where the discrete values at fine-scale nodes p_{i_k} are entries of the vector $\boldsymbol{p}_i$, $i = 1, \ldots, n_{\boldsymbol{u}}^h$. Once the basis functions are computed, $\mathcal{S}^h$ and $\mathcal{V}^h$ are replaced by $\mathcal{S}^H = \text{span}\left\{ \boldsymbol{N}_i^H, i = 1, \ldots, n_{\boldsymbol{u}}^H + n_{\bar{\boldsymbol{u}}}^H \right\}$ and $\mathcal{V}^H = \text{span}\left\{ \boldsymbol{N}_i^H, i = 1, \ldots, n_{\boldsymbol{u}}^H \right\}$, respectively. Then, the system for the coarse-scale displacement-vector, $\boldsymbol{d}^H$, can be constructed as

$$K_H \boldsymbol{d}^H = \boldsymbol{f}^H, \tag{18}$$

where K_H is the coarse-scale stiffness matrix, and f^H is the coarse-scale load vector. Specifically, the stiffness matrix K_H is written as:

5
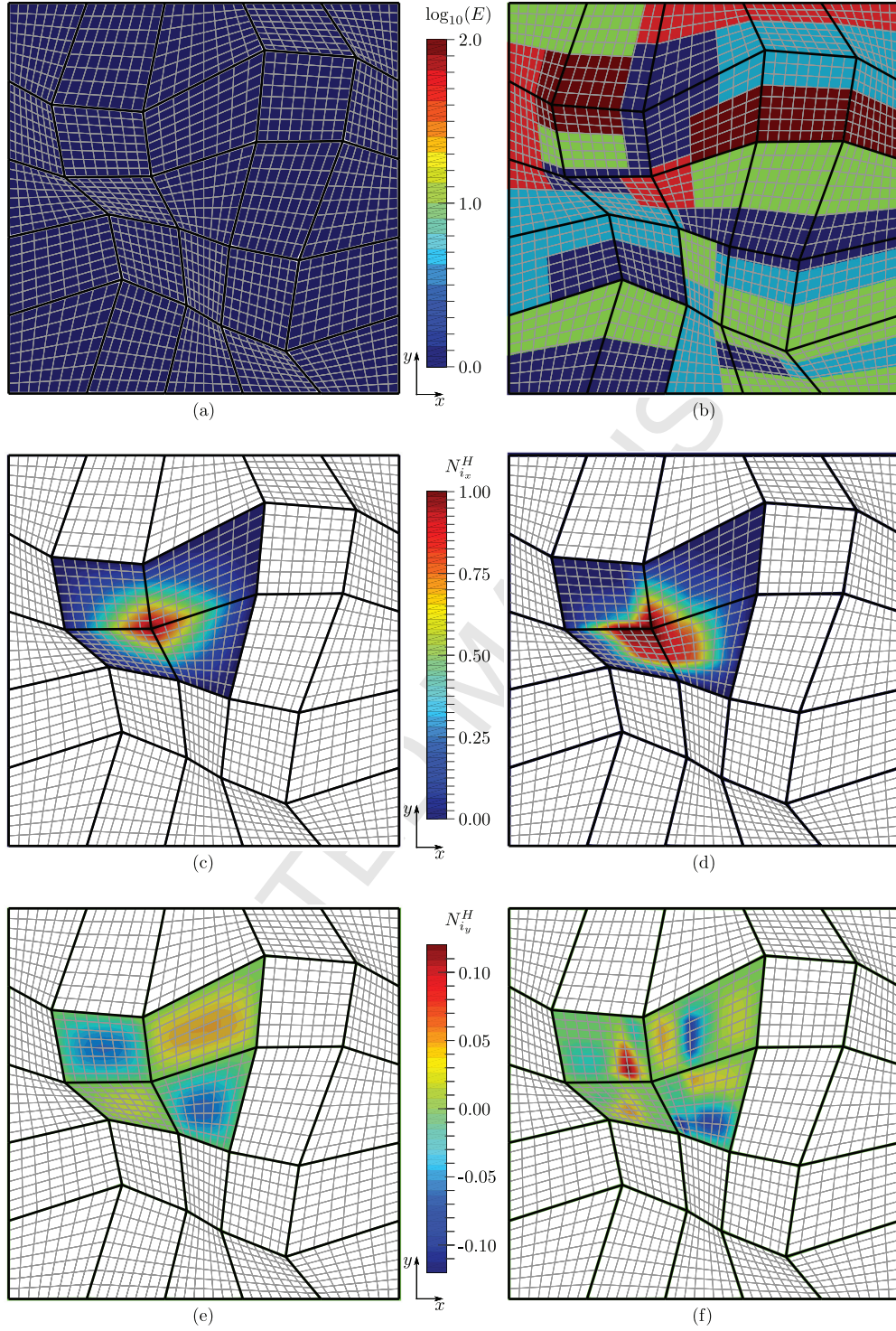
Figure 2: Coarse basis function $N_i^H = [N_{i_x}^H, N_{i_y}^H]^T$ associated to the DOF in the x-direction at the coarse mesh vertex V_4 in Fig. 1 for an homogeneous (left panels) and heterogeneous (right panels) medium. Distributions for Young's modulus, E, are shown in the top panels (a,b). A constant Poisson's ratio $\nu = 0.2$ is assumed in both cases. The x- and y-component of N_i^H are plotted in the middle (c,d) and bottom (e,f) panels respectively.

6

$$[K_H]_{i,j} = \int_\Omega \nabla^s N_i^H : \mathbf{C}_{dr} : \nabla^s N_j^H \ \mathrm{d}\Omega$$

$$= \int_\Omega \left(\sum_k^{n_u^h} p_{i_k} \nabla^s N_k^h \right) : \mathbf{C}_{dr} : \left(\sum_l^{n_u^h} p_{j_l} \nabla^s N_l^h \right) \mathrm{d}\Omega$$

$$= \boldsymbol{p}_i^T K_h \boldsymbol{p}_j \qquad\qquad \forall (i,j) \in \left\{ 1, 2, \ldots, n_u^H \right\} \times \left\{ 1, 2, \ldots, n_u^H \right\}. \tag{19}$$

The coarse-scale load vector $\boldsymbol{f}^H$ is defined as

$$[\boldsymbol{f}^h]_i = \boldsymbol{p}_i^T f^h \qquad\qquad \forall i \in \left\{ 1, 2, \ldots, n_u^H \right\}. \tag{20}$$

The multiscale solution, $\boldsymbol{d}_{MS}^h$, for the system of algebraic equations (12) is obtained by first solving the coarse-scale system (18) for $\boldsymbol{d}^H$, and then using (16) to interpolate the solution back to the fine-scale.

3.2. Two-stage multiscale preconditioner

The multiscale procedure presented above can be used to obtain efficient, but approximate, fine-scale solutions for the displacement-vector. For many practical applications, one needs control on the level of accuracy of the multiscale solutions. In addition, the quality of the multiscale results depend highly on the quality of the localization assumption. Thus, we describe an iterative procedure that guarantees the quality of the results to any desired level. Specifically, a two-stage preconditioner for the linear system (12) is developed. The preconditioner combines the two main ingredients of a multilevel technique: (a) construction and solution of an accurate coarse-scale system based on the MSFE procedure, to resolve low-frequency errors, and (b) a fine-scale smoothing operator, which is used to rapidly damp the high-frequency error components.

The coarse-space basis functions for $\mathcal{V}^H$, i.e. $\boldsymbol{p}_i$ ($i = 1, \ldots, n_u^H$), form the prolongation operator

$$P_H^h = [\boldsymbol{p}_1, \ldots, \boldsymbol{p}_{n_u^H}] : \mathcal{V}^H \to \mathcal{V}^h \tag{21}$$

that transfers vectors associated with the coarse-grid $\mathcal{T}^H$ to the fine-grid $\mathcal{T}^h$. The transpose of P_H^h is the restriction operator

$$R_h^H = [\boldsymbol{p}_1, \ldots, \boldsymbol{p}_{n_u^H}]^T : \mathcal{V}^h \to \mathcal{V}^H \tag{22}$$

that takes vectors associated with $\mathcal{T}^h$ and defines the analogue vector in $\mathcal{T}^H$. From an implementation point of view, the coarse-scale system stiffness matrix (19) and load vector (20) can be conveniently obtained using their fine-scale counterpart, prolongation and restriction operators as $K_H = R_h^H K_h P_H^h$ and $f^H = R_h^H f^h$.

The multiscale solution $\boldsymbol{d}_{MS}^h$ can be formally written as:

$$\boldsymbol{d}_{MS}^h = P_H^h \boldsymbol{d}^H = P_H^h (K_H)^{-1} f^H = P_H^h (R_h^H K_h P_H^h)^{-1} R_h^H f^h, \tag{23}$$

which provides the expression of the multiscale preconditioner M_{MS}^{-1}, namely

$$M_{MS}^{-1} = P_H^h (R_h^H K_h P_H^h)^{-1} R_h^H. \tag{24}$$

A key factor for successful performance of M_{MS}^{-1} is the efficient solution of the coarse-mesh problem, which resolves low-frequency error components [23]. The multiscale basis functions, combined with an adequate coarsening level, allow for accurately capturing fine-scale features at the coarse level. Thus, the two-level strategy becomes a competitive option as opposed to the classic algebraic multigrid approach (AMG), in which several coarsening levels are introduced to capture all error modes. Note that aggressive coarsening techniques are typically used in AMG to reduce memory requirements [24]. In our implementation, the coarse system is solved with a direct solver. Also, we observe that for practical applications one does not have to converge to machine accuracy, but employ the two-stage preconditioner to maintain the quality of multiscale results.

It is easy to prove that the multiscale preconditioner is rank deficient, i.e. $\text{rank}(M_{MS}^{-1}) \leq n_u^H$, thus $\text{rank}(M_{MS}^{-1}K_h) \leq n_u^H$ [25, 26]. Since the coarse-scale system cannot span the fine-scale space, M_{MS}^{-1} is effective for tackling low-frequency errors only. Therefore M_{MS}^{-1} must be complemented by a fine-scale smoothing preconditioner M_{sm}^{-1} to remove the high frequency errors in a second correction step. The resulting two-stage preconditioner, M^{-1}, is described by its action on a vector $\mathbf{v}^h \in \mathbb{R}^{n_u^h}$. Computing $\mathbf{z}^h = M^{-1}\mathbf{v}^h$ requires:

$$\text{stage 1:} \quad \mathbf{z}_0^h = M_{MS}^{-1}\mathbf{v}^h \tag{25}$$

$$\text{stage 2:} \quad \mathbf{z}^h = \mathbf{z}_0^h + M_{sm}^{-1}\mathbf{r}_0^h \tag{26}$$

where $\mathbf{r}_0^h = \mathbf{v}^h - K_h\mathbf{z}_0$. The operator form of M^{-1} is

$$M^{-1} = M_{MS}^{-1} + M_{sm}^{-1}\left(I - K_h M_{MS}^{-1}\right). \tag{27}$$

Algorithm 1 summarizes the steps to construct M^{-1}. The sequence of operations required to apply M_{MS}^{-1} and M^{-1} to a vector are given in Algorithms 2 and 3, respectively. Note that even for $K_h = K_h^T$, $M_{MS}^{-1} = M_{MS}^{-T}$ and $M_{sm}^{-1} = M_{sm}^{-T}$, the preconditioner (27) is non-symmetric. Thus, M^{-1} can be used either within a stationary iterative scheme, such as Richardson iteration, or a non-symmetric Krylov subspace method, like generalized minimal residual (GMRES) or biconjugate gradient stabilized (BICGSTAB) methods.

From (26) it is clear that stage 2 consists of one iteration of the relaxation scheme $\mathbf{z}_k^h = (\mathbf{z}_{k-1}^h + M_{sm}^{-1}\mathbf{r}_{k-1}^h)$, with k the iteration counter and $\mathbf{r}_{k-1}^h = (\mathbf{v}^h - K_h\mathbf{z}_{k-1})$. If stage 2 is modified to account for a prescribed number of smoothing steps $n_{sm} > 1$, another preconditioner $M_{n_{sm}}^{-1}$ is obtained, and the following relationship applies for the preconditioning of a vector:

$$\mathbf{z}^h = M_{n_{sm}}^{-1}\mathbf{v}^h = M^{-1}\mathbf{v}^h + \sum_{k=2}^{n_{sm}} M_{sm}^{-1}\left(I - K_h M_{sm}^{-1}\right)\mathbf{r}_{k-2}^h. \tag{28}$$

Remark 3.2. Since an elastic constitutive behavior is considered for the porous medium in the present case, matrix K_h is symmetric positive definite (SPD). To obtain a symmetric version preconditioner M^{-1}, which allows for using a symmetric Krylov solvers such as conjugate gradient (CG), a pre-smoothing step is needed before stage 1, i.e. Eq. (25). Provided a symmetric smoother is used, it can be shown that the operator form for the resulting three-stage preconditioner reads:

$$M^{-1} = 2M_{sm}^{-1} - M_{sm}^{-1}K_h M_{sm}^{-1} + \left(I - M_{sm}^{-1}K_h\right)M_{MS}^{-1}\left(I - M_{sm}^{-1}K_h\right)^T. \tag{29}$$

Note that the non-symmetric preconditioner (27) can still be used in conjunction with generalized CG methods to solve SPD systems without preventing the convergence of the iterative process [27, 28]. Recent examples of non-symmetric preconditioned CG using multigrid- or reduced order model-based approaches are presented in [29] and [30], respectively.

Remark 3.3. Even though serial simulations only are discussed in Section 4, the method is naturally suited for efficient parallel implementation. In particular, the computation of the basis functions, i.e. the prolongation operator, can be carried out independently on separate processors [31].

Algorithm 1 M^{-1} PRECONDITIONER COMPUTATION

1. **Compute** P_H^h
2. **Compute** $R_h^H = (P_H^h)^T$
3. **Compute** $K_H = R_h^H K_h P_H^h$
4. **Factorize** $K_H = L_{K_H} U_{K_H}$ with a direct solver
5. **Compute** M_{sm}^{-1} as a fine-scale smoothing preconditioner of K_h

---

Algorithm 2 M_{MS}^{-1} PRECONDITIONER APPLICATION

---

1. **Input:** v^h; **Output:** $z^h = M_{MS}^{-1}v^h$
2. **Compute** $v^H = R_h^H v^h$
3. **Compute** $z^H = L_{K_H}^{-1}v^H$
4. **Compute** $v^H = U_{K_H}^{-1}z^H$
5. **Compute** $z^h = P_H^h v^H$

Algorithm 3 M^{-1} PRECONDITIONER APPLICATION

---

1. **Input:** v^h; **Output:** $z^h = M^{-1}v^h$
2. **Apply** M_{MS}^{-1} to v^h to get z_0^h
3. **Compute** $r_0^h = K_h z_0^h$
4. **Compute** $r_0^h \leftarrow v^h - r_0^h$
5. **Apply** M_{sm}^{-1} to r_0^h to get z^h
6. **Compute** $z^h \leftarrow z_0^h + z^h$

---

unknown DOFs in x-direction   unknown DOFs in y-direction

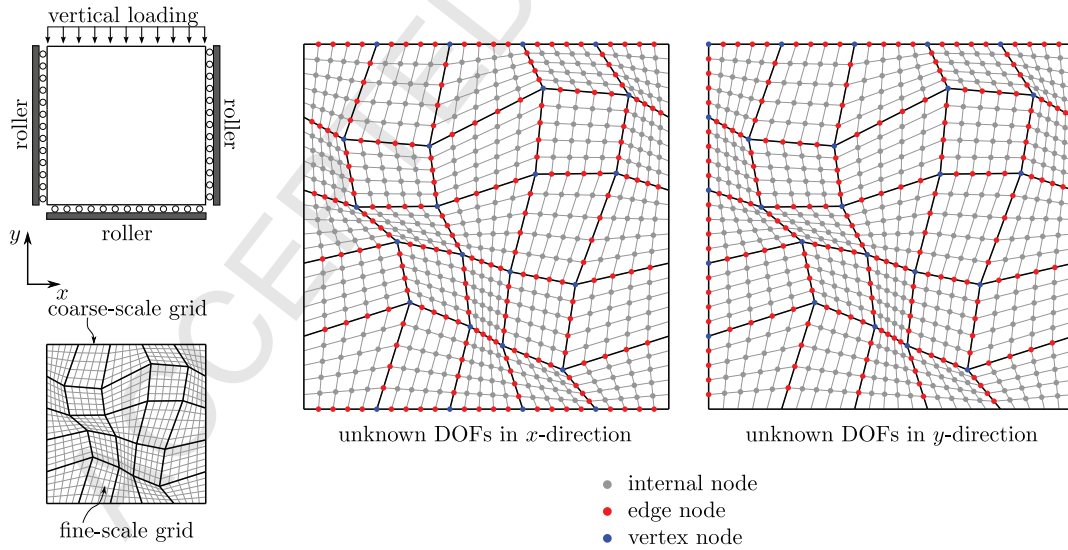- internal node
- edge node
- vertex node

Figure 3: Sketch of a one dimensional, laterally confined compression test and corresponding multiscale grid with the wire-basket ordering [21] for unknown DOFs in x- and y-direction, respectively.

9

3.3. Prolongation operator

The prolongation operator P_H^h is assembled directly from the basis functions (21) by solving local problems satisfying (17) for each coarse element. In addition, the relationship between multiscale methods and non-overlapping domain decomposition preconditioners [19, 32] proves very useful for an algebraic interpretation of the localization conditions (17b) and hence of the construction of the prolongation operator. Based on a wire-basket decomposition of the fine-scale problem [21], where W is the permutation matrix associated with the wire-basket permutation, the fine-scale system (12) can be rewritten as

$$\hat{K}_h \hat{d}^h = \hat{f}^h \tag{30}$$

with

$$\hat{K}_h = W^T K W = \begin{bmatrix} \hat{K}_{II} & \hat{K}_{IE} & \hat{K}_{IV} \\ \hat{K}_{EI} & \hat{K}_{EE} & \hat{K}_{EV} \\ \hat{K}_{VI} & \hat{K}_{VE} & \hat{K}_{VV} \end{bmatrix}, \qquad \hat{d}^h = W^T d^h = \begin{bmatrix} \hat{d}_I \\ \hat{d}_E \\ \hat{d}_V \end{bmatrix}, \qquad \hat{f}^h = W^T d^h = \begin{bmatrix} \hat{f}_I \\ \hat{f}_E \\ \hat{f}_V \end{bmatrix}. \tag{31}$$

The subscripts I, E, and V denote the internal, edge, and vertex DOFs as shown in Fig. 3. Gaussian elimination of the first block row leads to:

$$\begin{bmatrix} \hat{K}_{II} & \hat{K}_{IE} & \hat{K}_{IV} \\ 0 & \hat{S}_{EE} & \hat{S}_{EV} \\ 0 & \hat{S}_{VE} & \hat{S}_{VV} \end{bmatrix} \begin{bmatrix} \hat{d}_I \\ \hat{d}_E \\ \hat{d}_V \end{bmatrix} = \begin{bmatrix} I & 0 & 0 \\ -\hat{K}_{EI}\hat{K}_{II}^{-1} & I & 0 \\ -\hat{K}_{VI}\hat{K}_{II}^{-1} & 0 & I \end{bmatrix} \begin{bmatrix} \hat{f}_I \\ \hat{f}_E \\ \hat{f}_V \end{bmatrix}, \tag{32}$$

where $\hat{S}_{ij}$ are the blocks of the Schur complement matrix $\hat{S}$, i.e.,

$$\hat{S} = \begin{bmatrix} \hat{S}_{EE} & \hat{S}_{EV} \\ \hat{S}_{VE} & \hat{S}_{VV} \end{bmatrix}, \qquad \hat{S}_{ij} = \hat{K}_{ij} - \hat{K}_{iI}\hat{K}_{II}^{-1}\hat{K}_{Ij}, \qquad \forall (i,j) \in \{E,V\} \times \{E,V\}. \tag{33}$$

The second block row in (32), in which internal information is interpolated onto the edge and vertices nodes via the terms involving $\hat{K}_{II}^{-1}$, is approximated by the reduced boundary condition (17b), namely

$$\tilde{K}_{EE}\hat{d}_E + \tilde{K}_{EV}\hat{d}_V = \mathbf{0}, \tag{34}$$

which neglects the influence of the right-hand side term, with $\hat{S}_{EE} \approx \tilde{K}_{EE}$ and $\hat{S}_{EV} \approx \tilde{K}_{EV}$. For the plane-strain configuration, matrices $\tilde{K}_{EE}$ and $\tilde{K}_{EV}$ are obtained by assembling the local contributions (A.7) given in Appendix A. Ignoring $\hat{f}_I$ and replacing $\hat{d}_V$ by d^H, (32) and (34) allow for computing $\hat{d}_E$ and $\hat{d}_I$ as a function of d^H

$$\hat{d}_E = -\tilde{K}_{EE}^{-1}\tilde{K}_{EV}\hat{d}^H = P_{EV}d^H, \qquad \hat{d}_I = \tilde{K}_{II}^{-1}\left(-\hat{K}_{IE}P_{EV} - \hat{K}_{IV}\right)d^H = P_{IV}d^H. \tag{35}$$

Finally, the prolongation (21) and restriction (22) operators can now be rewritten using operators P_{EV} and P_{IV} as follows:

$$d^h = W \begin{bmatrix} \hat{d}_I \\ \hat{d}_E \\ d^H \end{bmatrix} = W \begin{bmatrix} P_{IV} \\ P_{EV} \\ I_{VV} \end{bmatrix} d^H \implies P_H^h = W \begin{bmatrix} P_{IV} \\ P_{EV} \\ I_{VV} \end{bmatrix}, \quad R_h^H = (P_H^h)^T = \begin{bmatrix} R_{VI}, R_{VE}, I_{VV} \end{bmatrix} W^T, \tag{36}$$

where I_{VV} is the identity matrix of size equal to number the vertex DOFs, $R_{VI} = P_{IV}^T$, and $R_{VE} = P_{EV}^T$.

Remark 3.4. The algebraic construction of the prolongation operator P_H^h, as described above, closely follows the derivation given [19] for flow through heterogeneous porous media. The difference between the two approaches lies in the formulation selected for the fine scale problem. In particular, the two-point flux approximation (TPFA) finite volume formulation used in [19] allows for obtaining the matrix form of the reduced boundary condition exclusively utilizing the specific wirebasket ordering matrix W and the fine-scale system K_h.

Remark 3.5. The coarse-scale system matrix K_H can be related to the Schur complement blocks (33). Using (36), K_H can be rewritten as

$$K_H = R_h^H K_h P_H^h = \begin{bmatrix} R_{VI}, R_{VE}, I_{VV} \end{bmatrix} \underbrace{W^T K_h W}_{\hat{K}_h} \begin{bmatrix} P_{IV} \\ P_{EV} \\ I_{VV} \end{bmatrix} = R_{VE}\hat{S}_{EE}P_{EV} + R_{VE}\hat{S}_{EV} + \hat{S}_{VE}P_{EV} + \hat{S}_{VV}. \tag{37}$$

If the exact Schur complement $\hat{S}$ is represented in a partially hierarchical basis [21, 33] as

$$\hat{S} = \begin{bmatrix} I_{EE} & 0 \\ -R_{VE} & I_{VV} \end{bmatrix} \bar{S} \begin{bmatrix} I_{EE} & -P_{EV} \\ 0 & I_{VV} \end{bmatrix}, \qquad\qquad \bar{S} = \begin{bmatrix} \bar{S}_{EE} & \bar{S}_{EV} \\ \bar{S}_{VE} & \bar{S}_{VV} \end{bmatrix}, \tag{38}$$

after some algebraic manipulation it can be seen that $\bar{S}_{EE} = \hat{S}_{EE}$, $\bar{S}_{EV} = (\hat{S}_{EE}P_{EV} + \hat{S}_{EV})$, $\bar{S}_{VE} = (R_{VE}\hat{S}_{EE} + \hat{S}_{VE})$, and $\bar{S}_{VV} = K_H$. If the approximations $\bar{S}_{EE} \approx \tilde{K}_{EE}$, $\bar{S}_{EV} \approx 0$ and $\bar{S}_{VE} \approx R_{VE}\tilde{K}_{EE}$ are introduced in (38) the following approximation for $\hat{S}$ is obtained:

$$\hat{S} \approx \begin{bmatrix} \tilde{K}_{EE} & \tilde{K}_{EV} \\ 0 & K_H \end{bmatrix}. \tag{39}$$

4. Numerical Results

In the numerical examples presented here, the algebraic system (12) is solved using the multiscale preconditioner described in Section 3.2. Richardson iteration and BICGSTAB are selected as solvers. The coarse-scale system is solved with a direct solver. The second stage consists of application of an incomplete LU factorization with a prescribed level of fill-in ℓ [23], ILU(ℓ), to the updated residual vector, with ℓ a nonnegative integer. Unless otherwise indicated, the no-fill ILU(0) preconditioner is used. The stopping criterion is based on the reduction of the relative L^2-norm of the residual [23]

$$\rho = \frac{\left\| f^h - K_h d_{MS}^h \right\|_2}{\left\| f^h \right\|_2} < \tau, \tag{40}$$

with a relative tolerance $\tau = 10^{-8}$. The coarsening ratio C_r, i.e.,

$$C_r = \frac{n_u^h}{n_u^H}, \tag{41}$$

is used as an indicator of the size of the coarse problem relative to fine-scale one. Since this work is primarily focused on developing the mathematical formulation of multiscale geomechanics, as a proof of concept, the performance of the method is assessed based on the iteration count, n_{it}. Future work would include performance studies based on CPU time for three-dimensional domains. We note that a single iteration for the Richardson method involves one matrix-vector product and one preconditioner application. On the other hand, a single BICGSTAB iteration requires two matrix-vector products, two preconditioner applications and four scalar products [23].

4.1. Heterogeneous synthetic case

4.1.1. Problem setup

An elastic isotropic medium with variable distribution of the elastic modulus $E(x)$ is considered. The domain is discretized using four meshes labeled cart, skew, trig, and rand. Each mesh is built on a reference 7×7 element uniform grid of quadrilaterals. First, corresponding base meshes for every type are defined: no distortion is introduced
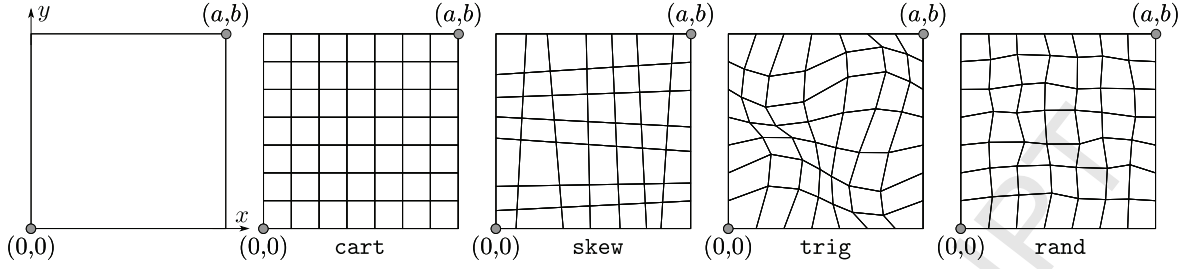
11

Figure 4: Heterogeneous synthetic case: physical domain (left) and different base meshes used in the numerical tests.

for mesh `cart`, coinciding with a standard Cartesian grid, while the remaining meshes are constructed by moving the positions $(\hat{x}, \hat{y})$ of the nodes of the base grid according to different strategies. Base meshes are shown in Fig. 4. The relationship used for base meshes `trig` and `rand` to remap positions $(\hat{x}, \hat{y})$ into (x, y) are

$$\underline{\text{base mesh } \texttt{trig}}: \begin{cases} x = \hat{x} + 0.1 \, \sin(2\pi\hat{x})\sin(2\pi\hat{y}), \\ y = \hat{y} + 0.1 \, \sin(2\pi\hat{x})\sin(2\pi\hat{y}), \end{cases} \qquad \underline{\text{base mesh } \texttt{rand}}: \begin{cases} x = \hat{x} + \Psi_x h, \\ y = \hat{y} + \Psi_y h, \end{cases} \tag{42}$$

with Ψ_x and Ψ_y uniformly distributed random variables ranging between -0.3 and 0.3. Then, final meshes are generated by five successive dyadic subdivision of the reference mesh, totaling 224×224 elements.

The geomechanical characterization is done in terms of dimensionless quantities. A layered Young's modulus distribution inspired by real well log data from an oil shale formation is considered. The original moduli sequence has been rescaled to have dimensionless maximum value $E_{max} = 1.0$ and minimum value $E_{min} = 1.0 \times 10^{-\beta}$, with β a scalar parameter, and mapped on each mesh as shown in Fig. 5. We consider jumps in E to three orders of magnitude, namely $\beta = 1$, 2, and 3. The homogeneous case, which is obtained by setting $\beta = 0$, is also addressed. A 0.2 Poisson's ratio is assigned to all elements. When not uniquely defined, the averaging criterion used here to determine E for the reduced boundary problem (17b) consists in taking the maximum value over adjacent elements sharing an edge [17].

As far as boundary conditions are considered, three sets are analyzed:

- *laterally constrained*: a roller support condition is assigned to all boundary Γ except for the top segment Γ_t where a uniform uniform vertical displacement $\bar{u}$ is prescribed

$$\boldsymbol{u} \cdot \boldsymbol{n} = -\bar{u} \qquad \qquad \text{on } \Gamma_t \tag{43a}$$
$$\boldsymbol{u} \cdot \boldsymbol{n} = 0 \qquad \qquad \text{on } \Gamma_l \cup \Gamma_b \cup \Gamma_r \tag{43b}$$
$$(\boldsymbol{\sigma} \cdot \boldsymbol{n}) \cdot \boldsymbol{m} = 0 \qquad \qquad \text{on } \Gamma_t \cup \Gamma_l \cup \Gamma_b \cup \Gamma_r \tag{43c}$$

- *laterally unconstrained*: same conditions as for the laterally constrained setup apply, except for the roller constraint over the right segment Γ_r that is here replaced by traction free conditions

$$\boldsymbol{u} \cdot \boldsymbol{n} = -\bar{u} \qquad \qquad \text{on } \Gamma_t \tag{44a}$$
$$\boldsymbol{u} \cdot \boldsymbol{n} = 0 \qquad \qquad \text{on } \Gamma_l \cup \Gamma_b \tag{44b}$$
$$(\boldsymbol{\sigma} \cdot \boldsymbol{n}) \cdot \boldsymbol{m} = 0 \qquad \qquad \text{on } \Gamma_t \cup \Gamma_l \cup \Gamma_b \tag{44c}$$
$$\boldsymbol{\sigma} \cdot \boldsymbol{n} = [0, 0]^T \qquad \qquad \text{on } \Gamma_r \tag{44d}$$

- *simple shear*: a fixed basement over Γ_b is assumed, with displacements in the *x*-direction varying linearly with
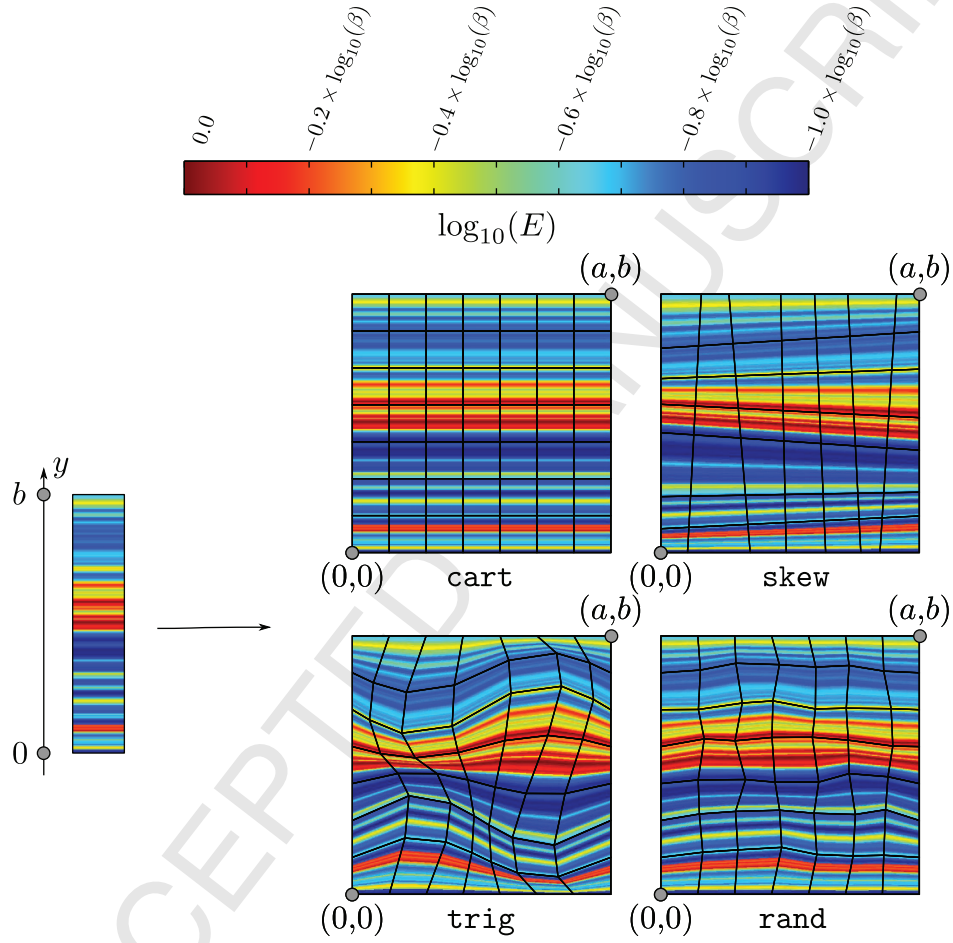
12

Figure 5: Heterogeneous synthetic case: base-10 logarithm of a layered Young modulus field (left) and its mapping on the fine-scale meshes used in the numerical tests. The base meshes are plotted in black.

13

y and displacements in the *y*-direction prevented everywhere over Γ

$$\boldsymbol{u} = [\bar{u}, 0]^T \qquad \text{on } \Gamma_t \qquad (45a)$$

$$\boldsymbol{u} \cdot \boldsymbol{n} = \frac{(y - a)}{b} \bar{u} \qquad \text{on } \Gamma_l \cup \Gamma_r \qquad (45b)$$

$$\boldsymbol{u} \cdot \boldsymbol{m} = 0 \qquad \text{on } \Gamma_l \cup \Gamma_r \qquad (45c)$$

$$\boldsymbol{u} = \boldsymbol{0} \qquad \text{on } \Gamma_b \qquad (45d)$$

In Eqs. (43)-(45) $\boldsymbol{m}$ is the unit tangent vector at the boundary and the boundary segments are given by $\Gamma_l = \{\boldsymbol{x} \in \Gamma \mid x = 0\}$, $\Gamma_b = \{\boldsymbol{x} \in \Gamma \mid y = 0\}$, $\Gamma_r = \{\boldsymbol{x} \in \Gamma \mid x = a\}$, and $\Gamma_t = \{\boldsymbol{x} \in \Gamma \mid y = b\}$. We consider the unit square domain, i.e. $a = 1.0$ and $b = 1.0$, and set $\bar{u} = -1^{-6}$. The above boundary condition sets are representative of three limit cases configurations that can be encountered in applications of practical interest in reservoir geomechanics: in the laterally constrained and unconstrained cases the volumetric contraction of the medium is the dominant deformation mechanism, while for the simple shear test the process is essentially driven by deviatoric strain-stress components. The fine-scale mesh consists of 50,625 nodes and 224×224 elements for a total number of DOFs $n_{\boldsymbol{u}}^h$ equal to 100,575, 100,800, and 99,450 for constrained, unconstrained, and simple shear case, respectively.

4.1.2. Multiscale solution

The quality of the original multiscale solution $\boldsymbol{d}_{MS}^h$—namely, an approximate, non-iterative solution—is first analyzed with respect to the fine-scale reference solution $\boldsymbol{d}_{ref}^h$. The accuracy is assessed both in terms of the relative residual norm, ρ, and the relative error, ε, defined based on the following normalized L^∞-norm

$$\varepsilon = \frac{\left\| \boldsymbol{d}_{ref}^h - \boldsymbol{d}_{MS}^h \right\|_\infty}{\left\| \boldsymbol{d}_{ref}^h \right\|_\infty} = \frac{\max_{i \in \{1,2,\dots,n_{\boldsymbol{u}}^h\}} \left| d_{ref,i}^h - d_{MS,i}^h \right|}{\max_{i \in \{1,2,\dots,n_{\boldsymbol{u}}^h\}} \left| d_{ref,i}^h \right|} \qquad (46)$$

with $d_{ref,i}^h$ and $d_{MS,i}^h$ the nodal components of $\boldsymbol{d}_{ref}^h$ and $\boldsymbol{d}_{MS}^h$, respectively. Profiles showing ε and ρ values for different test cases are given in Figs. 6-8 for a 7×7 coarse system. The adopted coarsening strategy, consisting in evenly agglomerating 32 fine-scale elements in *x*- and *y*-direction, leads to C_r equal to 967.1, 900.0, and 1,381.4 for constrained, unconstrained, and simple shear case, respectively.

For the homogeneous case, i.e. $\beta = 0$, the exact solution lies in the bilinear space spanned by the multiscale basis functions for the three boundary conditions sets irrespective of mesh type. Therefore multiscale and fine-scale reference solutions coincide. This is also the case for the heterogeneous laterally constrained setup when mesh `cart` is used since the sought solution is exactly approximated by piecewise linear interpolation in the *y*-direction. In the remaining tests, the multiscale solution does not match the fine-scale solution but still provides a fairly accurate estimate, the largest error ε values amounting to only a few percent for higher E contrasts. Also the relative residual exhibits a satisfactory behavior, always lower by more than three orders of magnitude.

Figure 9 shows a comparison between fine-scale reference and multiscale solution for the simple shear setup with mesh `skew` and $\beta = 3$. Contour plots of the relative residual *x*- and *y*-component are also provided. Notice that largest residuals are, as expected, localized over coarse mesh edges.

4.1.3. Multiscale preconditioner iterative solution

In this section we investigate the performance of the multiscale preconditioning strategy described in Section 3.2. First, we focus on mesh `skew` and consider a sequence of four coarse-scale problems starting from a 56×56 element coarse mesh, in which four fine-scale elements are agglomerated both in *x*- and *y*-direction. The other coarse-scale problems are constructed by progressively coarsening elements by a factor two in each direction. Beyond material heterogeneity and loading conditions, the effects of different local boundary conditions for the local problem (17) is also analyzed. In particular, we introduce local linear boundary conditions and compare the convergence behavior with the reduced ones computed by (17b).

Table 1 provides the iteration count as a function of β and the type of local boundary conditions when a single ILU(0) application is used as second stage preconditioner. BICGSTAB exhibits robust convergence behavior for the

14
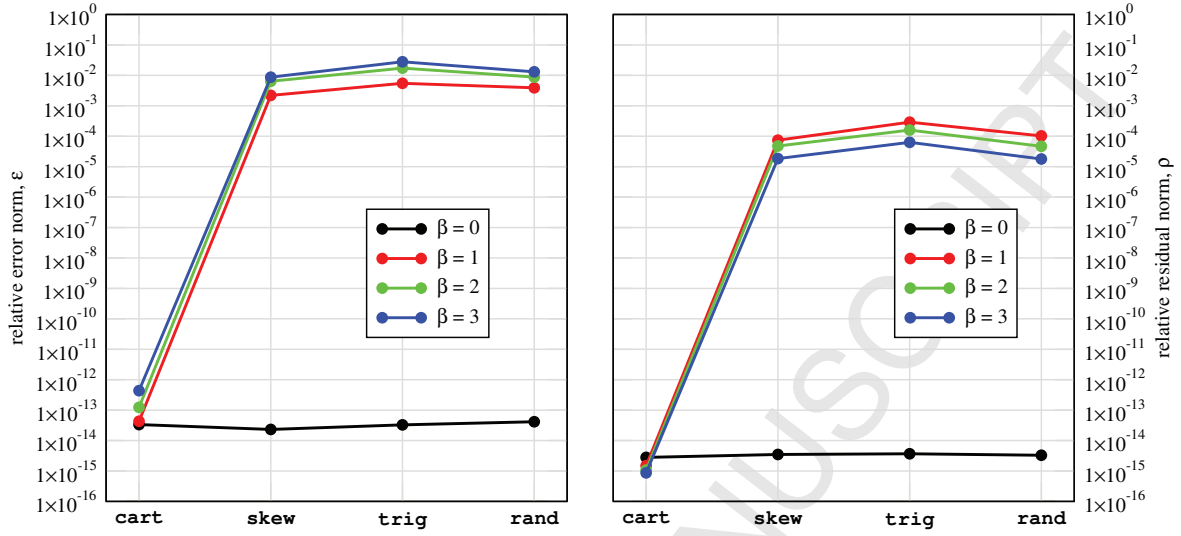
Figure 6: Heterogeneous synthetic case, laterally constrained test: relative error (left) and relative residual (right) of the multiscale solution after one iteration with no second stage smoothing for Young's modulus contrasts up to three order of magnitude ($\beta = 3$). Note that $\beta = 0$ denotes the homogeneous case. The fine-scale mesh consists of 50,625 nodes and 224×224 elements for a total number of DOFs equal to 100,575, 100,800, and 99,450 for constrained, unconstrained, and simple shear case, respectively. A 7×7 coarse mesh is used, which corresponds to a coarsening ratio $C_r = 967.1$.

Figure 7: Heterogeneous synthetic case: same as Fig. 6 for the laterally unconstrained test, with a coarsening ratio $C_r = 900.0$.

Figure 8: Heterogeneous synthetic case: same as Fig. 6 for the simple shear test, , with a coarsening ratio C_r=1,381.4.

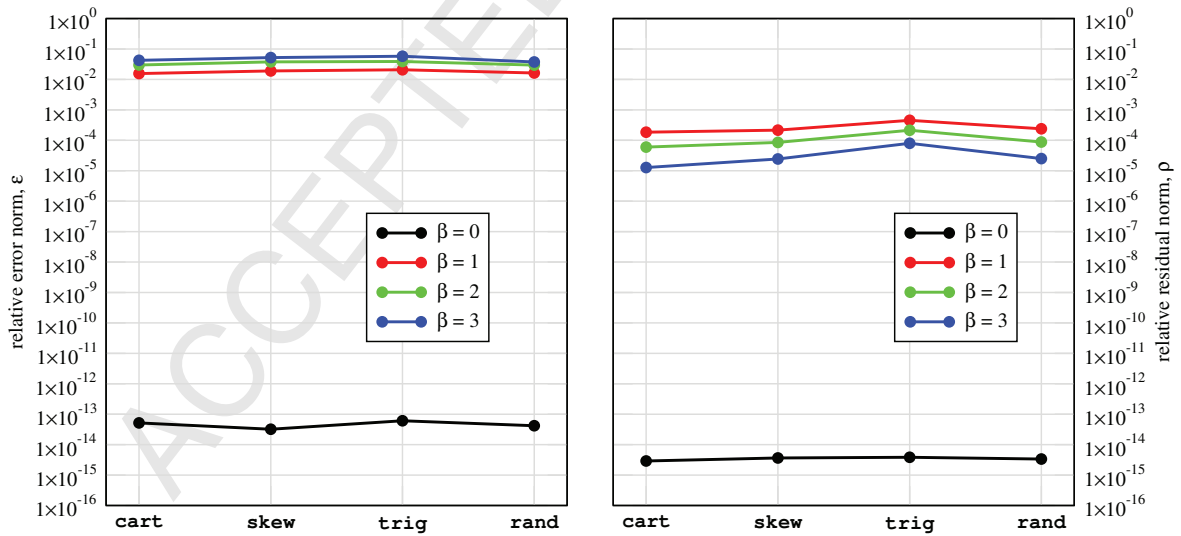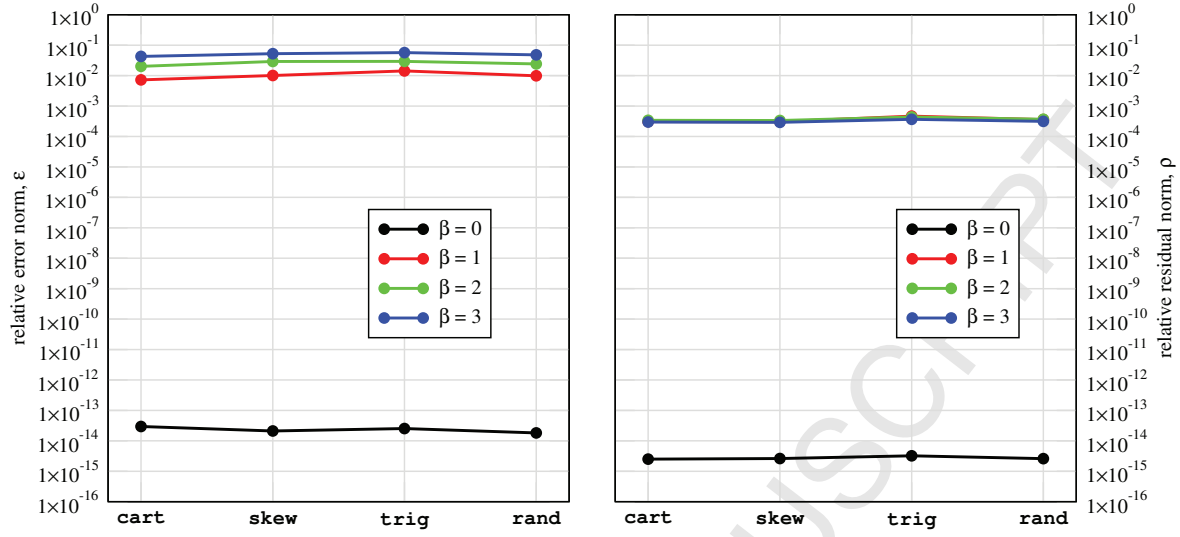entire stiffness range and loading conditions considered herein. Conversely, Richardson method appears extremely sensitive to an aggressive coarsening strategy, with the iteration number rapidly degrading. Indeed, as C_r grows, it appears evident the expected superior convergence rate for a Krylov-based scheme like BICGSTAB over a stationary iteration such as Richardson, which becomes totally impractical for the high C_r values. Although BICGSTAB iteration count increases approximately by a factor of ten between the smallest and largest coarsening ratios, this comes with the benefit of solving a much smaller coarse-scale system. As to the localization assumption, reduced boundary conditions produce best Richardson performance if low stiffness contrasts are considered ($\beta = 1$) while linear boundary conditions seem superior for higher contrasts ($\beta = 3$). No substantial impact on BICGSTAB is detected.

The convergence rate deterioration for higher coarsening ratio values can be substantially mitigated if ILU(0) is applied for several smoothing steps n_{sm} in the second preconditioning stage. Figs. 10- 11 display iteration counts for Richardson and BICGSTAB, respectively, with $n_{sm} = 1, 2, 4, 8$. A 7×7 coarse mesh is selected, which leads to a coarsening ratio C_r equal to 967.1, 900.0, and 1,381.4 for constrained, unconstrained, and simple shear case, respectively. Doubling n_{sm} produces an average n_{it} decrease of about 50% and 30% for Richardson and BICGSTAB, respectively. The optimal number for n_{sm} must be selected so that the additional computational cost involved in the second preconditioning stage is compensated by a lower overall solution time. Note that if GMRES is used instead of BICGSTAB, the iteration reduction is also beneficial, especially for large-size problems, because it corresponds a lower-dimensional basis for the Krylov space that has to be stored as the iteration progresses [23]. A systematic study of the optimal balance between coarsening level and iteration count leading to the best computational performance in terms of CPU time is out of the scope of the present study and it is the subject of ongoing research.

Richardson iteration performance is comparable with BICGSTAB only for the lowest coarsening strategy in which the ratio between average number of iterations for the different test cases in Richardson relative to BICGSTAB is on the order of two to three. Whenever significant coarsening is desired, BICGSTAB, or another Krylov-based scheme, should be the method of choice. Therefore, we only report BICGSTAB convergence history for meshes cart, trig and rand in Table 2. Reduced boundary conditions for the local problem are employed. The trend discussed above for mesh skew is observed for all meshes. Mesh trig is characterized by the most distorted layered structure, thus it is of no surprise that the worst performance is always associated with it.

4.2. Plane-strain subsidence

The preconditioner is here tested for a realistic application, simulating the steady-state deformation of a porous formation caused by a pore-pressure change in a productive formation. Plane-strain conditions are assumed. Two

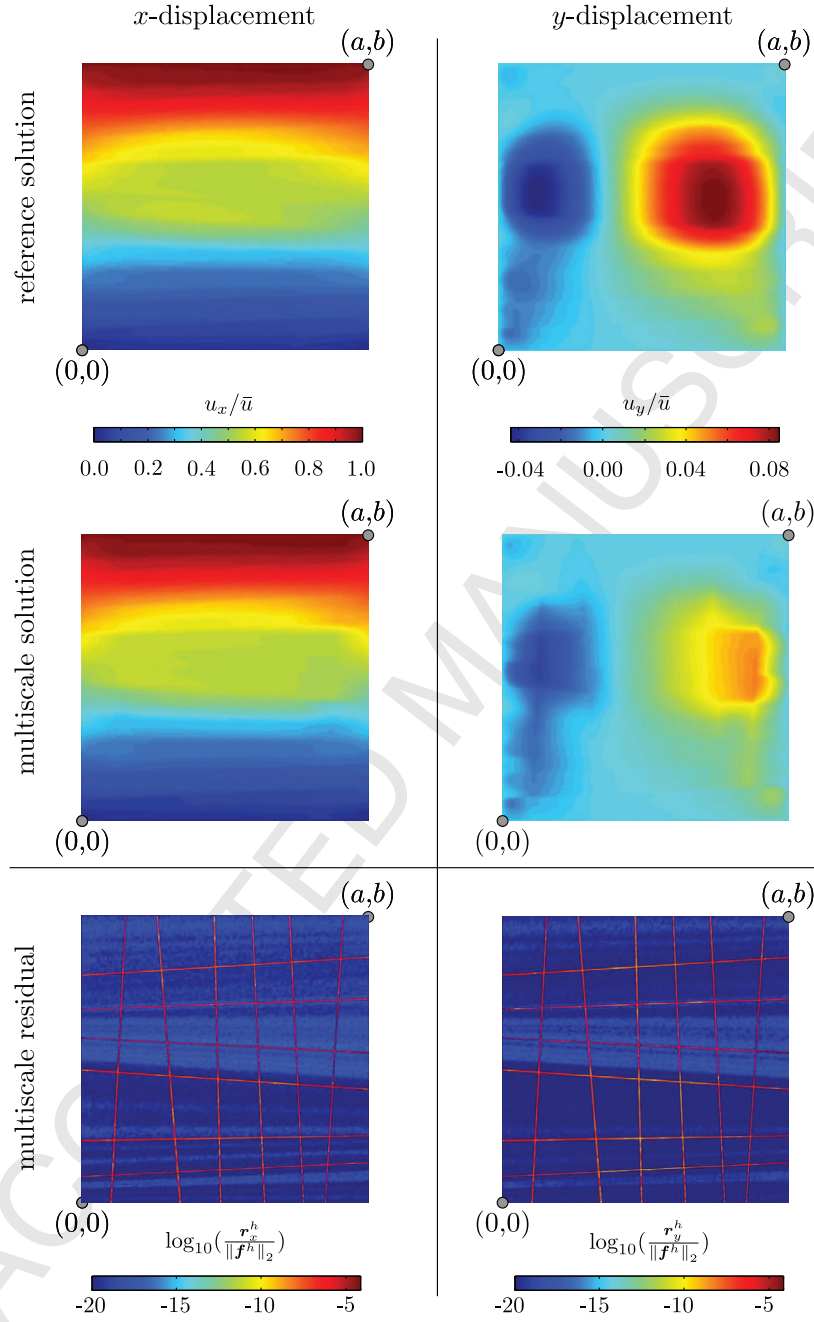Figure 9: Heterogeneous synthetic case (mesh skew, simple shear test, $\beta = 3$): fine-scale reference solution, multiscale solution after one iteration with no second stage smoothing and residual contour plot for the displacement field in x- (top panels) and y-direction (bottom panels), respectively. A 7×7 coarse mesh is used, that correspond to a coarsening ratio C_r of 1,381.4.

17

Table 1: Heterogeneous synthetic case: number of Richardson and BICGSTAB iterations to converge using mesh `skew` with Young's modulus contrasts up to three order of magnitude ($\beta = 3$). For each case case two iteration values are reported, the left and right one corresponding to using reduced and linear boundary conditions, respectively, for the local problem (17a). If different, best iteration performance is highlighted in bold. The fine-scale mesh consists of 50,625 nodes and 224×224 elements for a total number of DOFs equal to 100,575, 100,800, and 99,450 for constrained, unconstrained, and simple shear case, respectively. Four coarse meshes, that are obtained agglomerating 4, 8, 16, and 32 elements both in x- and y-direction, are used.

| β	# coarse elements	laterally constrained				laterally unconstrained				simple shear			
		Richardson		BICGSTAB		Richardson		BICGSTAB		Richardson		BICGSTAB	
1	56×56	**10**	13	**4**	5	13	13	5	5	**11**	15	5	5
	28×28	**33**	47	**7**	9	**41**	54	**8**	10	**41**	70	**9**	11
	14×14	**78**	107	**11**	15	**98**	111	**14**	15	**138**	228	**15**	20
	7×7	**390**	464	**28**	30	**541**	557	**29**	31	**450**	556	**27**	28
2	56×56	**10**	14	**4**	5	**15**	16	**5**	6	**13**	19	**5**	6
	28×28	**42**	51	**10**	11	**47**	54	**9**	12	**49**	97	**9**	12
	14×14	**80**	156	**13**	18	**94**	158	**15**	17	**261**	387	**22**	23
	7×7	644	**592**	**34**	43	958	**783**	44	**39**	727	**717**	**34**	39
3	56×56	**12**	21	**4**	7	**19**	27	**5**	8	**15**	28	6	6
	28×28	64	**63**	**9**	10	84	**63**	13	**11**	**73**	123	**12**	14
	14×14	**89**	297	**15**	19	**126**	297	**14**	21	**475**	634	**29**	33
	7×7	1,116	**773**	**32**	44	2,069	**1,196**	59	**48**	1,161	**842**	50	**45**
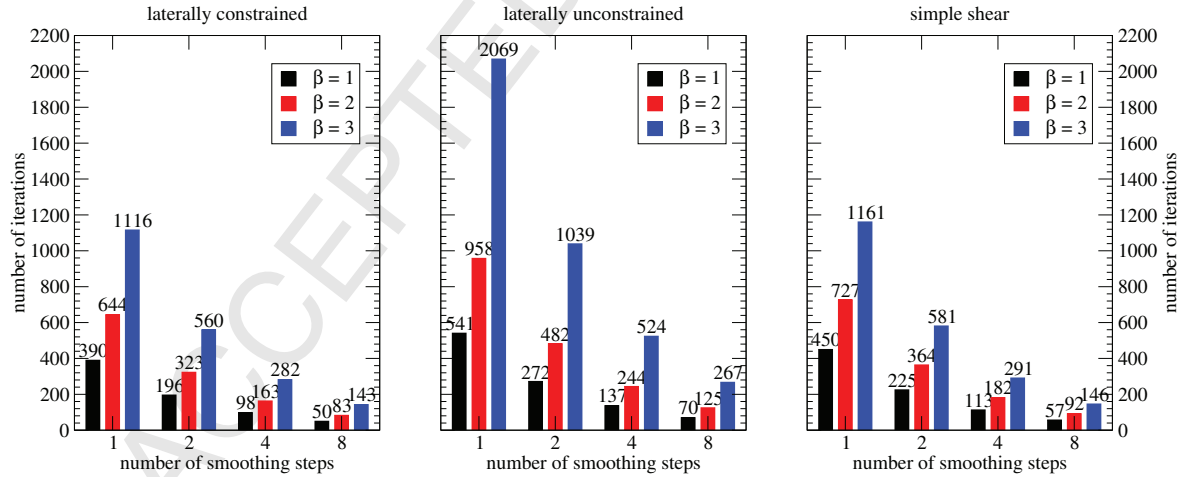
Figure 10: Heterogeneous synthetic case: number of Richardson iterations to converge for the laterally constrained (left panel), laterally unconstrained (middle panel), and simple shear setup (right panel) as a function of Young's modulus contrast (β) and the number of smoothing steps (n_{sm}). Iteration count is relative to mesh `skew` for a fixed coarsening ratio C_r equal to 967.1, 900.0, and 1,381.4 for constrained, unconstrained, and simple shear case, respectively, representative of a 7×7 element coarse-scale mesh.
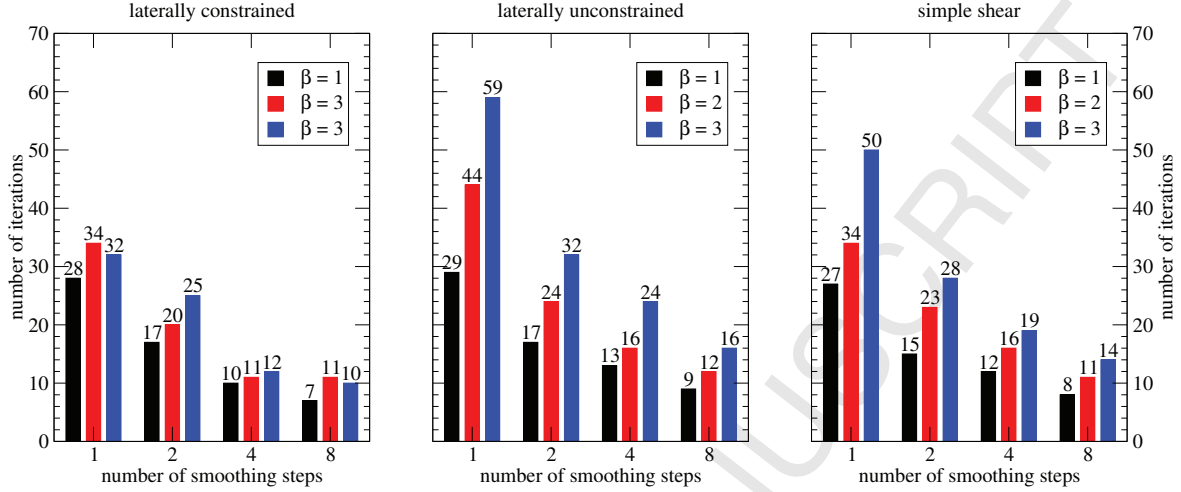
18

Figure 11: Heterogeneous synthetic case: same as Fig. 10 for BICGSTAB iterations.

Table 2: Heterogeneous synthetic case: number of BICGSTAB iterations to converge for Young's modulus contrasts up to three order of magnitude ($\beta = 3$). The fine-scale meshes consists of 50,625 nodes and 224×224 elements for a total number of DOFs equal to 100,575, 100,800, and 99,450 for constrained, unconstrained, and simple shear case, respectively. Four coarse meshes, that are obtained agglomerating 4, 8, 16, and 32 elements both in x- and y-direction, are used. The second stage preconditioner is a single application of ILU(0).

| β	# coarse	laterally constrained				laterally unconstrained				simple shear			
	elements	cart	skew	trig	rand	cart	skew	trig	rand	cart	skew	trig	rand
1	56×56	1	4	5	4	3	5	5	4	4	5	5	4
	28×28	1	7	9	7	9	8	10	8	7	9	10	8
	14×14	1	11	17	12	13	14	20	16	13	15	23	15
	7×7	1	28	27	24	23	29	31	31	27	27	34	29
2	56×56	1	4	5	4	4	5	5	5	4	5	5	4
	28×28	1	10	12	7	8	9	12	9	7	9	10	9
	14×14	1	13	17	13	14	15	17	16	18	22	25	21
	7×7	1	34	38	30	33	44	38	39	45	34	39	38
3	56×56	1	4	7	4	5	5	8	5	4	6	6	5
	28×28	1	9	16	10	9	13	20	11	11	12	15	11
	14×14	1	15	22	14	14	14	25	19	25	29	34	31
	7×7	1	32	62	41	45	59	70	52	51	50	63	46

19
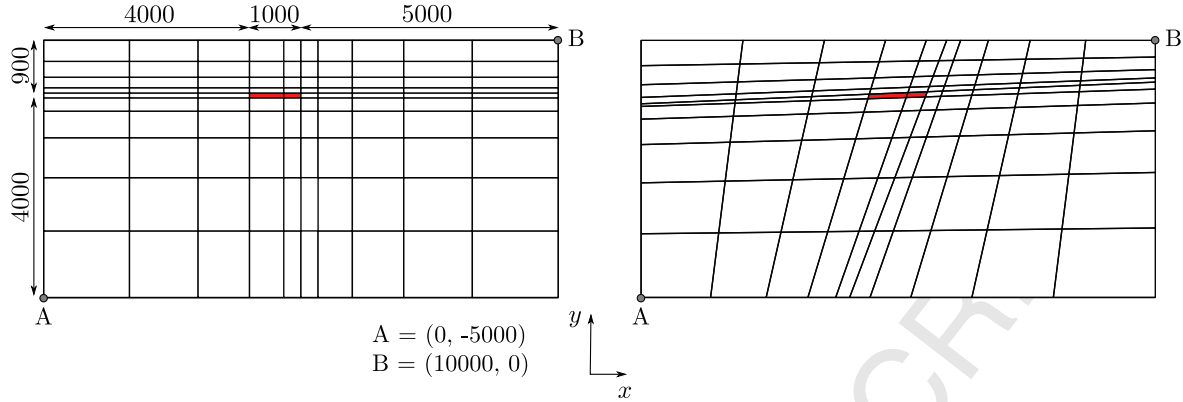
Figure 12: Plane-strain subsidence: base grid used to construct by subsequent dyadic subdivision the fine-scale mesh for the horizontal (left) and the tilted layering (right) configuration. The area corresponding to the reservoir is highlighted in red.

geometric configurations are considered, characterized by an horizontal and a tilted layering, respectively. Both grids share the same number of nodes and elements, with the tilted configuration obtained by remapping nodes in the horizontal orthotropic grid as shown in Fig. 12. Final meshes are generated by five successive dyadic subdivision of the base grid, leading to 320×320 elements in total. The compacting reservoir, highlighted in red in Fig. 12, is located at a depth of about 1,000 m, measuring approximately 1,000 m long and 100 m thick. The reservoir is completely sealed. We assume that production from the reservoir induces the largest possible pressure depletion $\Delta p = 100$ bar consistent with the reservoir depth in a normally pressurized basin, i.e. approximately $|y| \times 10^{-1}$ bar, with y in meters. Such pore pressure change field is specified as an external distributed source of strength for the mechanical model. The domain boundary is subject to roller constraints on all sides except from the ground surface which is assumed traction-free, i.e.,

$$\boldsymbol{u} \cdot \boldsymbol{n} = 0 \qquad \text{on } \Gamma_l \cup \Gamma_b \cup \Gamma_r \tag{47a}$$

$$\boldsymbol{\sigma} \cdot \boldsymbol{n} = [0, 0]^T \qquad \text{on } \Gamma_t \tag{47b}$$

$$(\boldsymbol{\sigma} \cdot \boldsymbol{n}) \cdot \boldsymbol{m} = 0 \qquad \text{on } \Gamma_l \cup \Gamma_b \cup \Gamma_r, \tag{47c}$$

where $\Gamma_l = \{\boldsymbol{x} \in \Gamma \mid x = 0\}$, $\Gamma_b = \{\boldsymbol{x} \in \Gamma \mid y = -5,000\}$, $\Gamma_r = \{\boldsymbol{x} \in \Gamma \mid x = 10,000\}$, and $\Gamma_t = \{\boldsymbol{x} \in \Gamma \mid y = 0\}$.

As far as the geomechanical characterization of the porous medium is concerned, four distributions of Young's modulus are prescribed based on the relationship for the vertical uniaxial compressibility c_M developed in [34]. Such constitutive law is representative of the deformation behavior of the normally consolidated formations of the Northern Adriatic basin, Italy, and has been used recently in a number of relevant real field applications, e.g [35–37]. The expression for c_M reads [36]

$$c_M = 0.01241 \left| \sigma_y' \right|^{-1.1342}, \tag{48}$$

with

$$\sigma_y' = \sigma_y + p = \underbrace{-0.12218 \, |y|^{1.0766}}_{\sigma_y} + \underbrace{0.1 \, |y|}_{p}. \tag{49}$$

where σ_y' is the vertical effective stress, σ_y is the vertical total stress, and p is the hydrostatic pressure. In (49) c_M is expressed in [bar^{-1}] unit, and σ_y', σ_y, and p are expressed in [bar] unit. Furthermore, an average Poisson ratio ν is
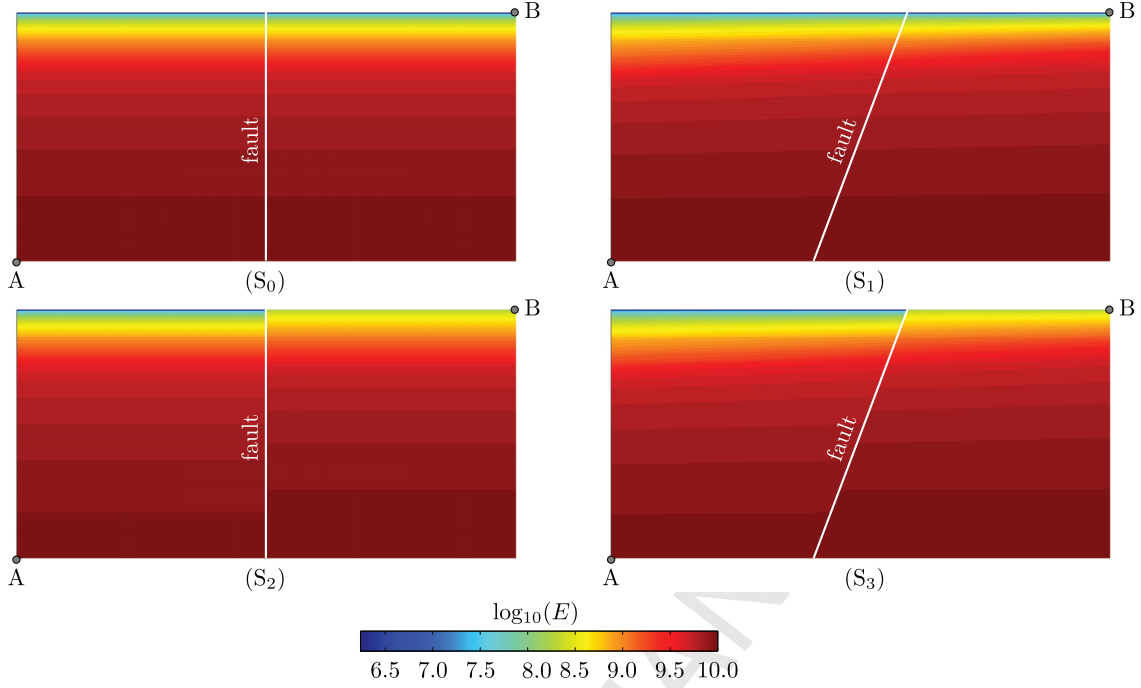
20

Figure 13: Plane-strain subsidence: base-10 logarithm contour plot of the Young modulus for the analyzed scenarios.

Table 3: Plane-strain subsidence: accuracy of the multiscale solution after one iteration without second stage smoothing for Scenarios S_0 to S_3. The fine-scale meshes consists of 103,041 nodes and 320×320 elements for a total number of DOFs $n_u^h = 205,119$. The same 10×10 coarse mesh is used, that corresponds to a coarsening ratio C_r of 981.4.

S_0		S_1		S_2		S_3	
ε	ρ	ε	ρ	ε	ρ	ε	ρ
2.88×10^{-1}	4.10×10^{-1}	2.50×10^{-1}	4.06×10^{-1}	2.89×10^{-1}	4.13×10^{-1}	2.50×10^{-1}	4.08×10^{-1}

set to 0.3 everywhere, which is a most representative value for the northern Adriatic basin [38]. Note that Young's modulus is computed from c_M and v as follows [22]

$$E = \frac{(1 - 2v)(1 + v)}{(1 - v)c_M}. \tag{50}$$

Four distributions for E are considered as shown in Fig. 13. It is assumed that the reservoir is bounded along the innermost vertical boundary by a sealing fault, across which a Young modulus discontinuity may occur. In the base case, S_0, E is assigned to each element according to the y-coordinate of its centroid. The same field is mapped onto the skewed grid in case S_1. In the remaining two scenarios, S_2 and S_3, a 100-m vertical offset of the geological layers located on the right of the fault is prescribed. As a result, the right portion of the domain is characterized by a stiffer medium, E being computed in S_2 by incrementing the centroid depth of each element by 100 m. Moduli in S_3 are again assigned projection from S_2. Note that fault activation is not considered in the present study, i.e. a continuum approach is used; for recent works on modeling fault mechanics, see [39, 40]. For the reduced boundary problem (17b) the same averaging criterion for the heterogeneous synthetic case is used.

Similar as for the synthetic heterogeneous test case, first the quality of the multiscale non-iterative solution is assessed. Table 3 reports ε and ρ values for Scenarios S_0-S_3 for the multiscale solution using a coarse mesh with
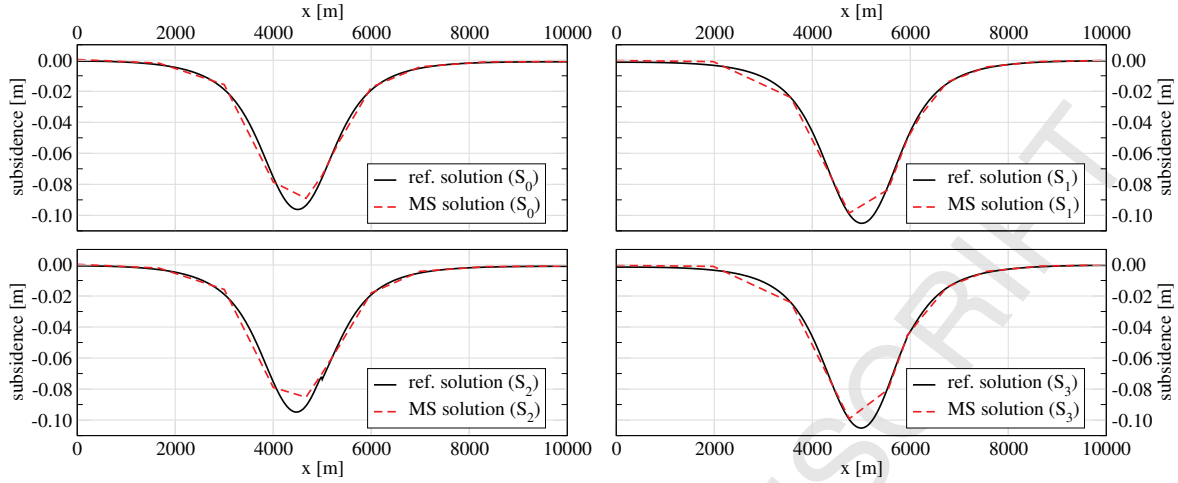
21

Figure 14: Plane-strain subsidence: ground vertical displacement profile for Scenarios S_0 to S_3. A continuous and a broken profiles are used for the fine-scale reference and the multiscale solution, respectively.

10×10 elements in each Scenario. An error ε ranging between 25% and 29% is observed. However, the multiscale solution allows for a quite reliable estimate of the subsidence experienced by the ground surface above the depleted formation as shown in Fig. 14.

Now, the performance of the iterative solution is investigated. Because of the strong stiffness heterogeneity combined with unfavorable aspect ratios of many elements, the ILU(0) preconditioner may represent too crude approximation of the fine-scale matrix K_h. This can result in either slow or lack of convergence. Such undesired behavior is due to several different reasons that depend on both the unstable computation and the unstable application of and approximate triangular factors [41]. Indeed, the asymptotic convergence of any linear stationary method, such as Richardson, requires the spectral radius of the iteration matrix to be smaller than 1. On the other hand, a Krylov method like BICGSTAB has no condition on the eigenspectrum of the preconditioned system matrix, and the convergence rate is mostly controlled by the degree of clustering of the eigenvalues, thus resulting in a more robust iterative procedure. Table 4 summarizes the convergence behavior for a single smoothing step. Using ILU(0) in the second stage results in a non-convergent Richardson iteration. Convergence for BICGSTAB is still achieved with ILU(0) smoothing. A convergent behavior is obtained for Richardson if ILU(2) in Scenarios S_0 and S_2, and ILU(6) in Scenarios S_1 and S_3 are employed. Again, performing additional smoothing steps proves beneficial in terms of total iteration count (Fig. 15).

5. Conclusions

In this work, a multiscale method for linear elastic geomechanics is developed. It is shown that the framework previously proposed for flow through porous media in [9, 19] can be generalized to the simulation of the mechanical response of heterogeneous geological formations. The multiscale method is constructed based on a FE formulation of the linear-momentum balance equation at fine-scale. A coarse-scale grid is superimposed to the fine-scale grid, on which local coarse-scale basis functions are computed enforcing decoupled local equilibrium element-wise. The basis functions provide the restriction and prolongation operators used to compute the coarse-scale systems for the displacement vector. A two-stage preconditioning strategy that couples the multiscale system with a smoother is devised for the iterative solution of the fine-scale linear system. The method is tested using a number of numerical experiments with synthetic and realistic geomechanical parameters. The numerical results demonstrate that the multiscale method is capable of providing accurate solutions. To improve the quality of the multiscale solutions, a two-stage iterative procedure is developed, where the multiscale stage is employed to resolve low-frequency errors. High-frequency errors are resolved in the second stage by an ILU-type smoother. The two-stage procedure is applied

22

Table 4: Plane-strain subsidence: number of BICGSTAB iterations to converge for Scenario S_0 to S_3 as a function of coarsening ratio C_r when a single smoothing step is performed in the second stage. The fine-scale mesh consists of 103,041 nodes and 320×320 elements for a total number of DOFs $n_{\bm{u}}^h = 205,119$.

| # coarse elements	$n_{\bm{u}}^H$	C_r	n_{it} (Richardson)				n_{it} (BICGSTAB)			
			S_0	S_1	S_2	S_3	S_0	S_1	S_2	S_3
			ILU(0)	ILU(0)	ILU(0)	ILU(0)	ILU(0)	ILU(0)	ILU(0)	ILU(0)
40×40	3,239	63.3	failed	failed	failed	failed	17	28	17	28
20×20	819	250.5	failed	failed	failed	failed	33	55	34	55
10×10	209	981.4	failed	failed	failed	failed	52	104	49	85
			ILU(2)	ILU(6)	ILU(2)	ILU(6)	ILU(2)	ILU(6)	ILU(2)	ILU(6)
40×40	3,239	63.3	54	236	50	249	11	9	11	9
20×20	819	250.5	714	189	255	198	22	18	21	20
10×10	209	981.4	759	280	289	283	33	30	32	33
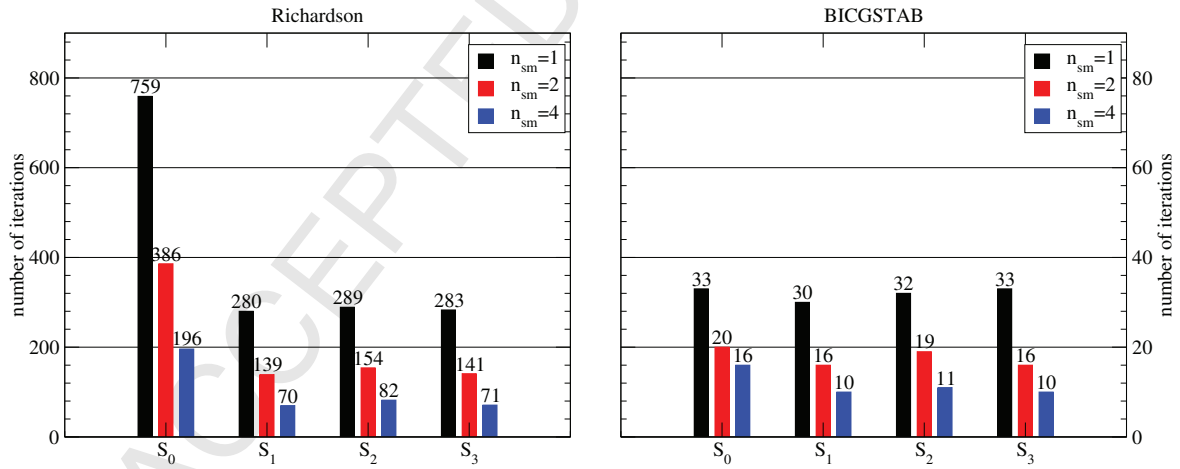
Figure 15: Plane-strain subsidence: number of iterations to converge for Scenarios S_0, S_1, S_2, and S_3 as a function of the number of smoothing steps n_{sm} for a fixed coarsening ratio $C_r = 981.4$ representative of a 10×10 element coarse-scale mesh. ILU(2) for scenarios S_0 and S_2, and ILU(6) for scenarios S_1 and S_3 are used as fine-scale smoothing precondition.

23

within a Krylov iteration, here BICGSTAB, to guarantee efficient convergence for challenging cases including those with distorted mesh and different boundary/loading conditions with a wide spectrum of the material parameters. The analysis builds confidence in the developed two-stage strategy as an effective preconditioner for real-field geomechanical simulation and encourages its integration in the well-established multiscale flow and transport simulation framework.

Acknowledgments

Appendix A. Reduced boundary problem for plane-strain elasticity

The reduced boundary problem (17b) is solved on a local reference system as shown in Fig. 1. A hat symbol, $\hat{()}$, is used to distinguish quantities expressed in the local reference system from those expressed in the global reference system. For simplicity, isotropic elasticity behavior is considered, i.e. the constitutive tensor $\mathbf{C}_{dr}$ is independent of the reference system. Using the classical Voigt notation [20] tensors and operators in (17b) are represented using matrix expressions, namely:

$$\mathbf{C}_{dr} = \begin{bmatrix} K_v & (K_v - 2G) & 0 \\ (K_v - 2G) & K_v & 0 \\ 0 & 0 & G \end{bmatrix}, \tag{A.1}$$

$$\hat{\nabla}\cdot = \begin{bmatrix} \frac{\partial}{\partial \hat{x}} & 0 & \frac{\partial}{\partial \hat{y}} \\ 0 & \frac{\partial}{\partial \hat{y}} & \frac{\partial}{\partial \hat{x}} \end{bmatrix}, \tag{A.2}$$

$$\hat{\nabla}_{\parallel}\cdot = \begin{bmatrix} \frac{\partial}{\partial \hat{x}} & 0 & 0 \\ 0 & 0 & \frac{\partial}{\partial \hat{x}} \end{bmatrix}, \tag{A.3}$$

$$\hat{\nabla}^s = \begin{bmatrix} \frac{\partial}{\partial \hat{x}} & 0 \\ 0 & \frac{\partial}{\partial \hat{y}} \\ \frac{\partial}{\partial \hat{y}} & \frac{\partial}{\partial \hat{x}} \end{bmatrix}, \tag{A.4}$$

$$\hat{\nabla}^s_{\parallel} = \begin{bmatrix} \frac{\partial}{\partial \hat{x}} & 0 \\ 0 & 0 \\ 0 & \frac{\partial}{\partial \hat{x}} \end{bmatrix}, \tag{A.5}$$

with $K_v = E(1 - \nu)/(1 + \nu)/(1 - 2\nu)]$ and $G = [E/2/(1 + \nu)]$ the uniaxial bulk modulus and the shear modulus, respectively. Using these expressions, the reduced boundary condition (17b) is expressed as

$$\begin{cases} \dfrac{\partial}{\partial \hat{x}}\left(K_v \dfrac{\partial \hat{N}^H_{i_{\hat{x}}}}{\partial \hat{x}}\right) = 0 \quad \text{(axial equilibrium)} \\ \dfrac{\partial}{\partial \hat{x}}\left(G \dfrac{\partial \hat{N}^H_{i_{\hat{y}}}}{\partial \hat{x}}\right) = 0 \quad \text{(transverse equilibrium)} \end{cases} \tag{A.6}$$

on ∂T_k, subject to the Dirichlet conditions as described in Eq. (17d). In essence, coarse mesh edges can be regarded as line elements for which axial extension and transverse simple shear effects are accounted for. Using the fine-scale basis functions to approximate N^H_i, the matrix form of Eq. (17b) is obtained as a sum of element contributions. For the edge element highlighted in red in Fig. 1, the contribution to be assembled in the global stiffness matrix reads

$$\tilde{K}_{E_i E_j} = Q^T \hat{\tilde{K}}_{E_i E_j} Q, \tag{A.7}$$

24

where

$$\hat{\tilde{K}}_{E_i E_j} = \frac{1}{l} \begin{bmatrix} K_v & 0 & -K_v & 0 \\ 0 & G & 0 & -G \\ -K_v & 0 & K_v & 0 \\ 0 & -G & 0 & G \end{bmatrix}, \tag{A.8}$$

$$Q = \begin{bmatrix} \cos\theta & \sin\theta & 0 & 0 \\ -\sin\theta & \cos\theta & 0 & 0 \\ 0 & 0 & \cos\theta & \sin\theta \\ 0 & 0 & -\sin\theta & \cos\theta \end{bmatrix}, \tag{A.9}$$

and $l = \left\| \hat{x}_{E_j} - \hat{x}_{E_i} \right\|_2$. Note that l is the edge length, and Q is an orthogonal transformation matrix needed to rotate vector quantities in the local reference system back into the global reference system [20].

References

[1] P. Jenny, S. H. Lee, H. A. Tchelepi, Multi-scale finite-volume method for elliptic problems in subsurface flow simulation, J. Comput. Phys. 187 (1) (2003) 47–67. doi:10.1016/S0021-9991(03)00075-5.

[2] P. Jenny, S. H. Lee, H. A. Tchelepi, Adaptive fully implicit multi-scale finite-volume method for multi-phase flow and transport in heterogeneous porous media, J. Comput. Phys. 217 (2) (2006) 627–641. doi:10.1016/j.jcp.2006.01.028.

[3] T. Y. Hou, X.-H. Wu, A Multiscale Finite Element Method for Elliptic Problems in Composite Materials and Porous Media, J. Comput. Phys. 134 (1) (1997) 169–189. doi:10.1006/jcph.1997.5682.

[4] Y. Efendiev, T. Y. Hou, Multiscale Finite Element Methods: Theory and Applications, Springer, New York, NY, USA, 2009. doi:10.1007/978-0-387-09496-0.

[5] H. A. Tchelepi, P. Jenny, S. H. Lee, C. Wolfsteiner, Adaptive Multiscale Finite-Volume Framework for Reservoir Simulation, SPE J. 12 (2) (2007) 188–195. doi:10.2118/93395-PA.

[6] H. Hajibeygi, G. Bonfigli, M. A. Hesse, P. Jenny, Iterative multiscale finite-volume method, J. Comput. Phys. 227 (19) (2008) 8604–8621. doi:10.1016/j.jcp.2008.06.013.

[7] H. Hajibeygi, P. Jenny, Multiscale finite-volume method for parabolic problems arising from compressible multiphase flow in porous media, J. Comput. Phys. 228 (14) (2009) 5129–5147. doi:10.1016/j.jcp.2009.04.017.

[8] R. Helmig, J. Niessner, B. Flemisch, M. Wolff, J. Fritz, Efficient Modeling of Flow and Transport in Porous Media Using Multiphysics and Multiscale Approaches, in: W. Freeden, M. Z. Nashed, T. Sonar (Eds.), Handbook of Geomathematics, Springer Berlin Heidelberg, Berlin, Heidelberg, 2010, pp. 417–457. doi:10.1007/978-3-642-01546-5_15.

[9] Y. Wang, H. Hajibeygi, H. A. Tchelepi, Algebraic multiscale solver for flow in heterogeneous porous media, J. Comput. Phys. 259 (2014) 284–303. doi:10.1016/j.jcp.2013.11.024.

[10] O. Møyner, K. Lie, A multiscale restriction-smoothed basis method for high contrast porous media represented on unstructured grids, J. Comput. Phys. 304 (2016) 46–71. doi:10.1016/j.jcp.2015.10.010.

[11] A. Kozlova, Z. Li, J. R. Natvig, S. Watanabe, Y. Zhou, K. Bratvedt, S. H. Lee, A Real-Field Multiscale Black-Oil Reservoir Simulator, in: SPE Reservoir Simulation Symposium, Society of Petroleum Engineers, 2015. doi:10.2118/173226-MS.

[12] H. W. Zhang, Z. D. Fu, J. K. Wu, Coupling multiscale finite element method for consolidation analysis of heterogeneous saturated porous media, Adv. Water Resour. 32 (2) (2009) 268–279. doi:10.1016/j.advwatres.2008.11.002.

[13] H. W. Zhang, J. K. Wu, J. Lv, A new multiscale computational method for elasto-plastic analysis of heterogeneous materials, Comput. Mech. 49 (2) (2012) 149–169. doi:10.1007/s00466-011-0634-1.

[14] H. W. Zhang, Y. Liu, S. Zhang, J. Tao, J. K. Wu, B. S. Chen, Extended multiscale finite element method: its basis and applications for mechanical analysis of heterogeneous materials, Comput. Mech. 53 (4) (2014) 659–685. doi:10.1007/s00466-013-0924-x.

[15] J. Aarnes, T. Y. Hou, Multiscale domain decomposition methods for elliptic problems with high aspect ratios, Acta Math. Appl. 18 (1) (2002) 63–76. doi:10.1007/s102550200004.

[16] M. Buck, O. Iliev, H. Andrä, Multiscale finite element coarse spaces for the application to linear elasticity, Cent. Eur. J. Math. 11 (4) (2013) 680–701. doi:10.2478/s11533-012-0166-8.

[17] M. Buck, O. Iliev, H. Andrä, Multiscale Finite Elements for Linear Elasticity: Oscillatory Boundary Conditions, in: J. Erhel, J. M. Gander, L. Halpern, G. Pichot, T. Sassi, O. Widlund (Eds.), Domain Decomposition Methods in Science and Engineering XXI, Springer International Publishing, 2014, pp. 237–245. doi:10.1007/978-3-319-05789-7_20.

[18] N. Spillane, V. Dolean, P. Hauret, F. Nataf, C. Pechstein, R. Scheichl, Abstract robust coarse spaces for systems of PDEs via generalized eigenproblems in the overlaps, Numer. Math. 126 (4) (2014) 741–770. doi:10.1007/s00211-013-0576-y.

[19] H. Zhou, H. A. Tchelepi, Two-Stage Algebraic Multiscale Linear Solver for Highly Heterogeneous Reservoir Models, SPE J. 17 (2) (2012) 523–539. doi:10.2118/141473-PA.

[20] T. J. R. Hughes, The Finite Element Method: Linear Static and Dynamic Finite Element Analysis, Dover Publications, 2000.

[21] B. F. Smith, P. E. Bjørstad, W. D. Gropp, Domain Decomposition: Parallel Multilevel Methods for Elliptic Partial Differential Equations, Cambridge University Press, Cambridge, UK, 1996.

[22] H. F. Wang, Theory of Linear Poroelasticity, Princeton University Press, Princeton, NJ, USA, 2000.

25

[23] Y. Saad, Iterative Methods for Sparse Linear Systems, 2nd Edition, Society for Industrial and Applied Mathematics, Philadelphia, PA, USA, 2003. `doi:10.1137/1.9780898718003`.

[24] K. Stüben, A review of algebraic multigrid, J. Comput. Appl. Math. 128 (1–2) (2001) 281–309. `doi:10.1016/S0377-0427(00)00516-1`.

[25] H. Zhou, Algebraic multiscale finite-volume methods for reservoir simulation, Phd thesis, Stanford University, USA (2010).

[26] H. Zhou, H. A. Tchelepi, Operator-Based Multiscale Method for Compressible Flow, SPE J. 13 (2) (2008) 267–273. `doi:10.2118/106254-PA`.

[27] O. Axelsson, Iterative Solution Methods, Cambridge University Press, Cambridge, UK, 1994. `doi:10.1017/CBO9780511162410`.

[28] R. Blaheta, GPCG–generalized preconditioned CG method and its use with non-linear and non-symmetric displacement decomposition preconditioners, Numer. Linear Algebr. Appl. 9 (6-7) (2002) 527–550. `doi:10.1002/nla.295`.

[29] H. Bouwmeester, A. Dougherty, A. V. Knyazev, Nonsymmetric Preconditioning for Conjugate Gradient and Steepest Descent Methods, Procedia Comput. Sci. 51 (2015) 276–285. `doi:10.1016/j.procs.2015.05.241`.

[30] D. Pasetto, M. Ferronato, M. Putti, A reduced order model-based preconditioner for the efficient solution of transient diffusion equations, Int. J. Numer. Meth. Eng. n/a (2016) n/a–n/a. `doi:10.1002/nme.5320`.

[31] A. M. Manea, J. Sewall, H. A. Tchelepi, Parallel Multiscale Linear Solver for Highly Detailed Reservoir Models, SPE J. X (2016) XX–XX. `doi:10.2118/173259-PA`.

[32] J. M. Nordbotten, P. E. Bjøstad, On the relationship between the multiscale finit volume method and domain decomposition preconditioners, Comput. Geosci. 13 (3) (2008) 367–376. `doi:10.1007/s10596-007-9066-6`.

[33] A. Toselli, O. Widlund, Domain Decomposition Methods - Algorithms and Theory, Springer Series in Computational Mathematics, Springer, Berlin, Germany, 2005. `doi:10.1007/b137868`.

[34] D. Baù, M. Ferronato, G. Gambolati, P. Teatini, Basin-scale compressibility of the northern Adriatic by the radioactive marker technique, Geotechnique 52 (8) (2002) 605–616. `doi:10.1680/geot.2002.52.8.605`.

[35] P. Teatini, N. Castelletto, M. Ferronato, G. Gambolati, L. Tosi, A new hydrogeologic model to predict anthropogenic uplift of Venice, Water Resour. Res. 47 (12) (2011) W12507. `doi:10.1029/2011WR010900`.

[36] N. Castelletto, G. Gambolati, P. Teatini, Geological CO2 sequestration in multi-compartment reservoirs: Geomechanical challenges, J. Geophys. Res.-Sol. Ea. 118 (5) (2013) 2417–2428. `doi:10.1002/jgrb.50180`.

[37] N. Castelletto, P. Teatini, G. Gambolati, D. Bossie-Codreanu, O. Vinckè, J.-M. Daniel, A. Battistelli, M. Marcolini, F. Donda, V. Volpi, Multiphysics modeling of CO_2 sequestration in a faulted saline formation in Italy, Adv. Water Resour. 62, Part C (2013) 570–587. `doi:10.1016/j.advwatres.2013.04.006`.

[38] P. Teatini, D. Baù, G. Gambolati, Water–gas dynamics and coastal land subsidence over Chioggia Mare field, northern Adriatic Sea, Hydrogeol. J. 8 (5) (2000) 462–479. `doi:10.1007/s100400000092`.

[39] B. Jha, R. Juanes, Coupled multiphase flow and poromechanics: A computational model of pore pressure effects on fault slip and earthquake triggering, Water Resour. Res. 5 (2014) 3776–3808. `doi:10.1002/2013WR015175`.

[40] A. Franceschini, M. Ferronato, C. Janna, P. Teatini, A novel Lagrangian approach for the stable numerical simulation of fault and fracture mechanics, J. Comput. Phys. 314 (2016) 503–521. `doi:10.1016/j.jcp.2016.03.032`.

[41] E. Chow, Y. Saad, Experimental study of ILU preconditioners for indefinite matrices, J. Comp. Appl. Math. 86 (2) (1997) 387–414. `doi:10.1016/S0377-0427(97)00171-4`.